HIGH ORDER METHODS FOR SUPERSONIC REACTIVE FLOWS

AFSOR GRANT FA9550-05-1-0123

FINAL REPORT

David Gottlieb
Division of Applied Mathematics
Brown University, Providence, Rhode Island

Wai Sun Don
Division of Applied Mathematics
Brown University, Providence, Rhode Island

Abstract

During the grant period, we have developed the high order methods, namely spectral methods, WENO-Z finite difference methods and the Hybrid spectral-WENO finite difference scheme for supersonic reactive and non-reactive flows. High order methods are needed in these kind of problems because the numerical solutions contain small scales that are important in the simulations of turbulence in interface instability and combustion in modeling combustors. Also since most of the relevant problems are not steady, long term integrations have to be carried out. It is well known that high order accuracy methods are needed in this situation.

We consider the problem of supersonic reactive flow in recessed cavities and simulate it by spectral multidomain techniques. This is important as a flameholder mechanism in scramjets. We have developed a multi-domain spectral method with stable and conservative penalty interface conditions for the numerical simulation of supersonic reactive recessed cavity flows with homogeneous grid.

The multi-domain hybrid Spectral-WENO finite difference method is introduced for the numerical solution of two dimensional nonlinear hyperbolic systems in a Cartesian physical domain which is partitioned into a grid of rectangular subdomains. The main idea of the Hybrid scheme is to conjugate the spectral and WENO methods for solving problems with shock or high gradients such that the scheme adapts its solver spatially and temporally depending on the smoothness of the solution in a

REPORT DOCUMENTATION PAGE

Form Approved
OMB No. 0704-0188

1. REPORT DATE *(DD-MM-YYYY)*	2. REPORT TYPE	3. DATES COVERED *(From - To)*
6/25/08	Final Technical Report	2/15/05-12/31/07

4. TITLE AND SUBTITLE
High Order Accuracy Methods for Supersonic Reactive Flows

5a. CONTRACT NUMBER

5b. GRANT NUMBER
FA9550-05-1-0123

5c. PROGRAM ELEMENT NUMBER

6. AUTHOR(S)
David Gottlieb and Wai-Sun Don

5d. PROJECT NUMBER

5e. TASK NUMBER

5f. WORK UNIT NUMBER

7. PERFORMING ORGANIZATION NAME(S) AND ADDRESS(ES)
Division of Applied Mathematics
182 George St.
Providence, RI 02912

8. PERFORMING ORGANIZATION REPORT NUMBER
4

9. SPONSORING/MONITORING AGENCY NAME(S) AND ADDRESS(ES)
Air Force Office of Scientific Research
875 North Arlington St., Suite 325, Room 3112
Arlington, VA 22203-1768

10. SPONSOR/MONITOR'S ACRONYM(S)

11. SPONSOR/MONITOR'S REPORT NUMBER(S)

12. DISTRIBUTION/AVAILABILITY STATEMENT
A

13. SUPPLEMENTARY NOTES

14. ABSTRACT
A multi-domain spectral methods with stable and conservative penalty interface conditions for the numerical simulation of supersonic reactive recessed cavity flows with inhomogeneous grid is developed. The high order hybrid Spectral-WENO finite difference method under multi-domain framework is also introduced for the numerical solution of of two dimensional nonlinear hyperbolic conservation laws in a Cartesian physical domain. A different approach in attempting to get more meaningful results is to model statistically those scales that can not be resolved. Methods for modeling those scales are being developed and applied. Numerical issues, such as boundary conditions, are being addressed and a new boundary procedure is being presented.

15. SUBJECT TERMS

16. SECURITY CLASSIFICATION OF:			17. LIMITATION OF ABSTRACT	18. NUMBER OF PAGES	19a. NAME OF RESPONSIBLE PERSON
a. REPORT	b. ABSTRACT	c. THIS PAGE			David Gottlieb
					19b. TELEPHONE NUMBER *(Include area code)*
					401-863-2266

given subdomain. Built as a multi-domain method, an adaptive algorithm is used to keep the solutions parts exhibiting high gradients and discontinuities always inside WENO subdomains while the smooth parts of the solution are kept inside a spectral one, avoiding oscillations related to the well-known Gibbs phenomenon and increasing the numerical efficiency of the overall scheme. A higher order version of the multi-resolution analysis proposed by Harten is used to determine the smoothness of the solution in each subdomain. The Hybrid method is applied to the two-dimensional Shock-Vortex Interaction and the Richtmyer-Meshkov Instability (RMI) problems.

We also have developed a different approach in attempting to get more meaningful results is to model statistically those scales that can not be resolved. Methods for modeling those scales are being developed and applied. Numerical issues, as boundary conditions, are being addressed and new boundary procedure is being presented.

1 A weighted multi-domain spectral penalty method with inhomogeneous grid for supersonic injective cavity flows

Spectral methods have been actively used in the computational fluid dynamics community in the last decades due to the merit of high order accuracy maintained for long time integration. Spectral methods also have been applied to highly complex fluid systems and have been proved to yield accurate solutions even with the stiff or discontinuous spatial gradients. These systems include the supersonic shock bubble interactions [12], the supersonic cavity flows [11], and etc. The difficulty of implementing the spectral method to these complex fluid systems is to deal with the stiff or discontinuous spatial gradients successfully. The discontinuous solution is commonly found in most high speed fluid mechanical systems. The spectral approximation of such solutions yields spurious oscillations near the discontinuity, known as the Gibbs phenomenon. These Gibbs oscillations destroy both the accuracy and stability in general. The essential methodology to deal with such oscillations in the spectral solution is the spectral viscosity or filtering methods [5,16,20,23]. The filtering which is mathematically equivalent to the spectral viscosity method but practically more efficient, is used to stabilize the flow fields over the time integration. The filtering reduces the high order oscillations by attenuating the high modes in the solution in a smooth manner. The filtering method can be applied either globally or locally. By applying the filtering locally more accurate solution is obtained in the smooth region and the spurious oscillations in the neighborhood of the discontinuity is considerably reduced. Thus it is desirable to separate the locally non-smooth regions from the global smooth region. A multi-domain spectral method has been developed to address this problem

[8,11,13,14,17–19]. Once the physical domain is split into multiple subdomains, the proper interface conditions should be imposed at the domain interfaces. The simplest condition is obtained using the averaging method. With the averaging method, the flow field at the domain interface is given by the average of the two adjacent solutions across the interface. Thus the continuity of the solution is ensured with the averaging method. Although this method is simple and efficient to be implemented, it may cause the generation of nonphysical solutions at the interface if the two adjacent subdomains have different order of approximation or different domain length, i.e. if the grid system is inhomogeneous. We define the grid inhomogeneity as the grid configuration such that the grid resolutions between the adjacent subdomains across the domain interface are different. Such difference can be obtained by having each domain have different order of polynomials or different physical domain length. If the distribution of the subdomain grids is inhomogeneous, the stable interface conditions derived for the homogeneous grid system are not enough and one needs to find the conditions with which the spatial inhomogeneity can be addressed properly.

At the domain interface of two adjacent subdomains which have the degree of polynomials, N_1 and N_2 in $x-$direction, the ratio of the grid spacing Δx_1 to Δx_2 is approximately given by

$$\frac{\Delta x_2}{\Delta x_1} = \frac{\Delta^{II}}{\Delta^{I}} \cdot \frac{N_1^2}{N_2^2}, \tag{1}$$

where Δ^{I} and Δ^{II} are the domain lengths of the two subdomains. If the grid spacing ratio $\frac{\Delta x_2}{\Delta x_1}$ is different and far from unity, we consider it as the inhomogeneous grid. If $\frac{\Delta x_2}{\Delta x_1} = 1$, i.e. if the grid is homogeneous, the averaging method can play an efficient role as a stable interface condition. However, if the ratio is far from unity, the simple averaging interface condition can cause the growth at the domain interface. In the real computation, the values of N_1, N_2 and Δ^{I}, Δ^{II} are chosen such that $\frac{\Delta x_2}{\Delta x_1}$ becomes close to unity but in general $\frac{\Delta x_2}{\Delta x_1} \neq 1$. The current work centers around the development of the method dealing with the solution in inhomogeneous grid, i.e. when $\frac{\Delta x_2}{\Delta x_1} \neq 1$.

In [11], we performed a 2D direct numerical simulation (DNS) of the recessed cavity with the multi-domain spectral penalty method under the condition that the grid is *homogeneous*. For the homogeneous grid system, the size and the number of collocation points in each subdomain are the same in each dimension. In this study, we extend the previous work to the inhomogeneous grid system to consider the injector-cavity system with the local hydrogen fuel injector. The crucial part of the DNS of the injector-cavity system is to resolve the hydrogen jet injector without causing any instability or nonphysical growing modes at the domain interfaces. The ratio of the injector to the cavity length scale is about $O(10^{-1})$. We use a smaller subdomain with higher order polynomials to resolve the narrow jet. In Figure 1 the local do-

main configuration is given for the cavity flameholder with (left figure) and without (right figure) the injector. The local domain configuration shown in the right figure is the typical domain system used in [11] for which grid system is homogeneous. The grid system in the left figure is inhomogeneous as the local injector is in the narrow domain. In [11], the stability analysis has been done with the assumption that each subdomain has the same length but can have different polynomial orders. With different polynomial orders, the stability is still maintained. In this work, we further show that the stability can be also maintained with the different domain length. For the 2D DNS, we use the grid inhomogeneity mainly due to the different domain length with the same polynomial order in each domain.

The stability conditions can be derived with the inhomogeneous grid, but these are only necessary conditions. Consequently there can be a non-reflecting mode at the domain interface which can yield a growth in time. A weighted spectral penalty method is proposed in order to minimize such nonphysical reflecting modes at the inhomogeneous grid interfaces. We note that in [8] the multidomain spectral method has been also used for the localized incompressible stratified turbulence flows in which the strong adaptive averaging method has been used with the spectral filtering technique. In our work, we observe that the averaging method with the filtering technique does not yield a smooth profile across the inhomogeneous grid interface for the compressible supersonic flows. This is due to the fact that the averaging does not guarantee the stability for the inhomogeneous grid as shown in the following section. The characteristic decomposition type interface conditions also fail to provide the smooth solution across the inhomogeneous grid interfaces. The major developments of the current work are as follows. 1) A generalized conservative and stable penalty conditions are derived for the inhomogeneous grid. 2) The weighted spectral penalty method is developed to minimize the non-physical growth modes at the inhomogeneous domain interfaces.

Using the proposed weighted penalty method, we carry out the 2D DNS of the injector-cavity system with various recessed angles. Cavity is an efficient flame-holder of scramjet engine as it generates the self-sustained recirculation region. The hot radicals from the chemical reactions residing in the recirculation region reduce the induction time and consequently maintain the auto-ignition. For the continuous auto-ignition and better fuel efficiency, such recirculation region should be stable for long time. In addition to the recirculation, the self-sustained acoustic oscillations bouncing back and forth inside cavity disturb the recirculation generating pressure fluctuations. The geometry of cavity is an important parameter for maintaining a stable recirculation while reducing the pressure oscillations. It is shown in [11] that the recessed cavity flameholder reduces the pressure fluctuations inside cavity more considerably than the normal wall cavity. In this research we verify qualitatively that the recessed

4

cavity increases the stability of the recirculation and reduces the pressure fluctuations inside the recessed cavity with the hydrogen injector.
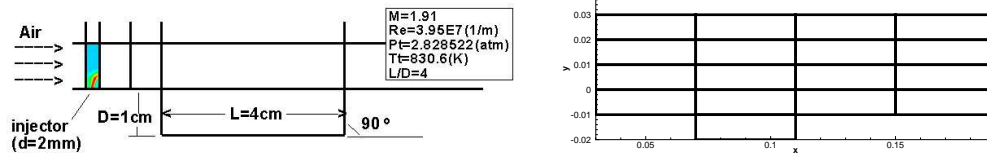

Fig. 1. Left: Local domain configuration of the normal injector-cavity flame-holder. Right: Local domain configuration of the normal cavity without injector. The initial physical configuration of the injector-cavity flame-holder is given in the legend box, where M denotes the Mach number, Re the normalized Reynolds number, P_t the baseline total pressure, T_t the baseline total temperature, and L/D the length to depth ratio of cavity.

The paper is organized as follows. In Section 2, a Legendre multi-domain spectral method with inhomogeneous grid is explained. Stability and conservativity are derived with the grid inhomogeneity. The generalized penalty interface conditions are derived accordingly. The weighted penalty method is proposed and various examples are illustrated. In Section 3, the governing equations and the injector-cavity system are briefly described. The numerical results from the simulation of the supersonic cavity flame-holder are provided. In this section, we verify that the proposed weighted spectral penalty method is applied successfully with the inhomogeneous grid of the injector-cavity system. The pressure fluctuations both in the normal and 30° wall cavities are presented. Concluding remarks with a brief future work outline are given in Section 4.

2 Multi-domain spectral method with inhomogeneous local mesh refinement

2.1 Conservative spectral penalty methods for inhomogeneous grid

In this section, we will consider the spectral penalty method for the inhomogeneous grid. We first consider the following one-dimensional conservation laws:

$$\frac{\partial q(x,t)}{\partial t} + \frac{\partial f(q(x,t))}{\partial x} = 0, \quad x \in \mathbf{R}, \quad t > 0. \tag{2}$$

Here $q(x,t)$ is the state vector and $f(q(x,t))$ is the flux vector. In [6] the conservative multi-domain Legendre method was proposed to approximate (2) on the Legendre

5

Gauss-Lobatto collocation points and such formulation was successfully used in [11]. In [6], theorems for the multi-domain Legendre penalty method have been provided under the assumption that each subdomain has the same domain length but the polynomial orders of approximation can be different. The different polynomial order in each domain makes the grid system inhomogeneous. Thus the same polynomial order has been used in [11] to avoid any numerical artifacts due to such inhomogeneity. In this paper, we will further generalize the previous formulation for fully inhomogeneous grid system.

For simplicity, we consider two subdomains $\Omega^I = [x_L, 0]$ and $\Omega^{II} = [0, x_R]$, for which the domain interface is at $x = 0$. In [11], $x_L = -x_R = -2$, but x_L and x_R can be different in this paper. Furthermore the left domain uses the polynomial order of N and the right domain of M and N is not necessarily the same as M. The Legendre multi-domain spectral penalty method is then given by

$$
\begin{aligned}
\frac{\partial q_N^I}{\partial t} + \frac{\partial I_N^I f(q_N^I)}{\partial x} = & \, \mathcal{B}(q_N^I(x_L, t)) + SV(q_N^I) + \\
& \tau_1 Q_N(x)[f^+(q_N^I(0, t)) - f^+(q_M^{II}(0, t))] + \\
& \tau_2 Q_N(x)[f^-(q_N^I(0, t)) - f^-(q_M^{II}(0, t))], \\
\frac{\partial q_M^{II}}{\partial t} + \frac{\partial I_M^{II} f(q_M^{II})}{\partial x} = & \, \mathcal{B}(q_M^{II}(x_R, t)) + SV(q_M^{II}) + \\
& \tau_3 Q_M(x)[f^+(q_M^{II}(0, t)) - f^+(q_N^I(0, t))] + \\
& \tau_4 Q_M(x)[f^-(q_M^{II}(0, t)) - f^-(q_N^I(0, t))].
\end{aligned}
\tag{3}
$$

Here q_N^I denotes the numerical approximation of $q(x, t)$ in Legendre polynomial of order N in Ω^I and q_M^{II} of order M in Ω^{II}. $\mathcal{B}$ is the boundary operator at the end points, i.e. $x = x_L, x_R$ and SV is the spectral vanishing-viscosity terms. I_N^I and I_M^{II} are the Legendre interpolation operators for the left and right subdomains respectively. Q_N and Q_M are the polynomials of order N and M respectively defined to vanish at the collocation points except at the boundary or interface points, that is, for Ω^I, $Q_N(x_i) = 0$ for $i = 1, \cdots, N-1$ and $Q_N(x_i) = 1$ for $i = 0, N$. The positive and negative fluxes f^+ and f^- are defined by

$$
f^\pm = \int S \Lambda^\pm S^{-1} dq,
\tag{4}
$$

with

$$
A \equiv \frac{\partial f}{\partial q} = S \Lambda S^{-1}.
\tag{5}
$$

The Jacobian matrix A is assumed to be symmetric. Λ^+ and Λ^- are the diagonal matrices composed of positive and negative eigenvalues of A respectively such as

$\Lambda = \Lambda^+ + \Lambda^-$. S and λ are the variables related to the characteristics and its direction of propagation. τ_1, τ_2, τ_3 and τ_4 are the penalty parameters and all are constants. As in [11], we assume that the boundary terms and the spectral vanishing-viscosity terms do not cause any instabilities and they do not appear in the following analysis. For the following theorems we define the discrete Legendre norm $(p, q)_N := \sum_{i=0}^{N} p(x_i) q(x_i) \omega_i$. x_i are the Legendre Gauss-Lobatto collocation points and $\omega_i = \frac{2}{N(N+1)[L_N(\xi(x_i))]^2}$ where ξ is the map from x to the Legendre Gauss-Lobatto points over $[-1, 1]$. If $pq \in P_{2N-1}$, the discrete sum is exact, i.e. $(p, q)_N = \int_{-1}^{1} p(\xi(x)) q(\xi(x)) d\xi$. In the following analysis, we define the weight vector $\vec{\omega}_N^I$ as the weight vector in Ω^I with $N + 1$ components such as $\vec{\omega}_N^I = (\omega_0^I, \cdots, \omega_N^I)^T$. We note that ω_N^I without the vector symbol denotes the last component of $\vec{\omega}_N^I$.

The scheme given in (3) is conservative if $x_L = -x_R = -2$ and the penalty parameters satisfy the following conditions

$$\tau_1 \omega_N^I - \tau_3 \omega_M^{II} = 1, \quad \tau_2 \omega_N^I - \tau_4 \omega_M^{II} = 1. \tag{6}$$

Here we note that there is a typo in the first equation of Eq. (23) on page 332 in [11]. The second term in the equation should not be $\tau_1 \omega_M^{II}$ but should be $\tau_3 \omega_M^{II}$ as given in the theorem above.

The scheme (3) is stable if $x_L = -x_R = -2$ and the penalty parameters satisfy the followings

$$2\tau_1 \omega_N^I \leq 1, \quad 2\tau_2 \omega_N^I \geq 1, \quad 2\tau_3 \omega_M^{II} \leq -1, \quad 2\tau_4 \omega_M^{II} \geq -1, \tag{7}$$
$$\tau_1 \omega_N^I - \tau_3 \omega_M^{II} = 1, \quad \tau_2 \omega_N^I - \tau_4 \omega_M^{II} = 1. \tag{8}$$

Here note that the scheme is stable even though the grid system is inhomogeneous, i.e. $N \neq M$.

If each subdomain has the same domain interval Δ, then the stability conditions are given by, defining $\Delta_2 = 2/\Delta$,

$$2\tau_1 \omega_N^I \leq \Delta_2, \quad 2\tau_2 \omega_N^I \geq \Delta_2, \quad 2\tau_3 \omega_M^{II} \leq -\Delta_2, \quad 2\tau_4 \omega_M^{II} \geq -\Delta_2,$$
$$\tau_1 \omega_N^I - \tau_3 \omega_M^{II} = \Delta_2, \quad \tau_2 \omega_N^I - \tau_4 \omega_M^{II} = \Delta_2.$$

Proof: The proof is done easily using the fact that for Ω^I,

$$(\vec{\omega}^I, \frac{\partial I_N^I f(q_N^I)}{\partial x})_N = \int_{-1}^1 \frac{\partial I_N^I f(q_N^I)}{\partial x} d\xi = \frac{2}{\Delta} \int_{-1}^1 \frac{\partial I_N^I f(q_N^I)}{\partial \xi} d\xi = \frac{2}{\Delta}(f(0) - f(x_L)) \quad (9)$$

since $I_N^I f(q_N^I) \in P_{2N-1}$ and in the same way for Ω^{II}.

If the interval of each subdomain is different, then the scheme (3) is conservative if the following conditions are satisfied.

$$\frac{\Delta^I}{2} \tau_1 \omega_N^I - \frac{\Delta^{II}}{2} \tau_3 \omega_M^{II} = 1, \quad \frac{\Delta^I}{2} \tau_2 \omega_N^I - \frac{\Delta^{II}}{2} \tau_4 \omega_M^{II} = 1. \quad (10)$$

Proof: Multiply the equations for q_N^I and q_M^{II} in (3) by $\vec{\omega}_M^I = (\omega_0^I, \cdots, \omega_N^I)^T$ and $\vec{\omega}_M^{II} = (\omega_0^{II}, \cdots, \omega_M^{II})^T$. Then using the Legendre quadrature rule we have

$$\int_{x_L}^0 \frac{\partial q_N^I}{\partial t} dx + \int_0^{x_R} \frac{\partial q_M^{II}}{\partial t} dx = -\int_{x_L}^0 \frac{\partial f_N^I}{\partial x} dx - \int_0^{x_R} \frac{\partial f_M^{II}}{\partial x} dx$$
$$+ \frac{\Delta^I}{2} \tau_1 [f^+(q_N^I(0,t))\omega_N^I - f^+(q_M^{II}(0,t))\omega_N^I]$$
$$+ \frac{\Delta^I}{2} \tau_2 [f^-(q_N^I(0,t))\omega_N^I - f^-(q_M^{II}(0,t))\omega_N^I]$$
$$+ \frac{\Delta^{II}}{2} \tau_3 [f^+(q_M^{II}(0,t))\omega_0^{II} - f^+(q_N^I(0,t))\omega_0^{II}]$$
$$+ \frac{\Delta^{II}}{2} \tau_4 [f^-(q_M^{II}(0,t))\omega_0^{II} - f^-(q_N^I(0,t))\omega_0^{II}].$$

Using the fact that $\int \frac{\partial f_N}{\partial x} dx = f^+ + f^-$ and $\omega_0^{II} = \omega_M^{II}$, we have the RHS of the above equation without the boundary terms become

$$RHS = f^+(q_N^I(0,t))[\frac{\Delta^I}{2} \tau_1 \omega_N^I - \frac{\Delta^{II}}{2} \tau_3 \omega_M^{II} - 1] + f^+(q_M^{II}(0,t))[\frac{\Delta^{II}}{2} \tau_3 \omega_M^{II} - \frac{\Delta^I}{2} \tau_1 \omega_N^I + 1] +$$
$$f^-(q_N^I(0,t))[\frac{\Delta^I}{2} \tau_2 \omega_N^I - \frac{\Delta^{II}}{2} \tau_4 \omega_M^{II} - 1] + f^-(q_M^{II}(0,t))[\frac{\Delta^{II}}{2} \tau_4 \omega_M^{II} - \frac{\Delta^I}{2} \tau_2 \omega_N^I + 1].$$

For any $f^\pm(0,t)$ (note that $f^\pm(q_N^I(0,t)) \neq f^\pm(q_M^{II}(0,t))$ in general), the RHS vanishes if the conditions Eq. (10) are satisfied. $\square$

The scheme (3) is stable if

$$2\tau_1\omega_N^I \le \frac{2}{\Delta^I}, \quad 2\tau_3\omega_M^{II} \le -\frac{2}{\Delta^{II}}, \quad 2\tau_2\omega_N^I \ge \frac{2}{\Delta^I}, \quad 2\tau_4\omega_M^{II} \ge -\frac{2}{\Delta^{II}}, \tag{11}$$

$$(\tau_1\omega_N^I - \tau_3\omega_M^{II})^2 - 2(\tau_1\omega_N^I\frac{2}{\Delta^{II}} - \tau_3\omega_M^{II}\frac{2}{\Delta^I}) + \frac{2}{\Delta^I}\frac{2}{\Delta^{II}} \le 0,$$

$$(\tau_2\omega_N^I - \tau_4\omega_M^{II})^2 - 2(\tau_2\omega_N^I\frac{2}{\Delta^{II}} - \tau_4\omega_M^{II}\frac{2}{\Delta^I}) + \frac{2}{\Delta^I}\frac{2}{\Delta^{II}} \le 0, \tag{12}$$

Proof: Multiplying each of Eq. (3) by $\vec{q}^I$ and $\vec{q}^{II}$, then the energy $E(t) = \frac{2}{\Delta^I}\int_{x_L}^0 q^2(x,t)dx + \frac{2}{\Delta^{II}}\int_0^{x_R} q^2(x,t)dx$ becomes

$$\frac{1}{2}\frac{dE(t)}{dt} = (\tau_1\omega_N^I - \frac{2}{\Delta^I}\frac{1}{2})\alpha_0^+ - (\tau_1\omega_N^I + \tau_3\omega_M^{II})\gamma_0^+ + (\tau_3\omega_M^{II} + \frac{2}{\Delta^{II}}\frac{1}{2})\beta_0^+$$

$$+ (\tau_2\omega_N^I - \frac{2}{\Delta^I}\frac{1}{2})\alpha_0^- - (\tau_2\omega_N^I + \tau_4\omega_M^{II})\gamma_0^- + (\tau_4\omega_M^{II} + \frac{2}{\Delta^{II}}\frac{1}{2})\beta_0^-,$$

where $\alpha_0^\pm = ((q_N^I(0,t))^T A^\pm q_N^I(0,t), \beta_0^\pm = (q_M^{II}(0,t))^T A^\pm q_M^{II}(0,t)$, and $\gamma_0^\pm = (q_N^I(0,t))^T A^\pm q_M^{II}(0,t)$. To make the RHS less than or equal to zero, first, the coefficients of the 2nd order terms corresponding the positive flux (negative flux) should be non-positive (non-negative) which provides the first conditions in Eq. (12). Also, the determinant each of the quadratic equations should be non-positive. This provides the second conditions Eq. (12). □
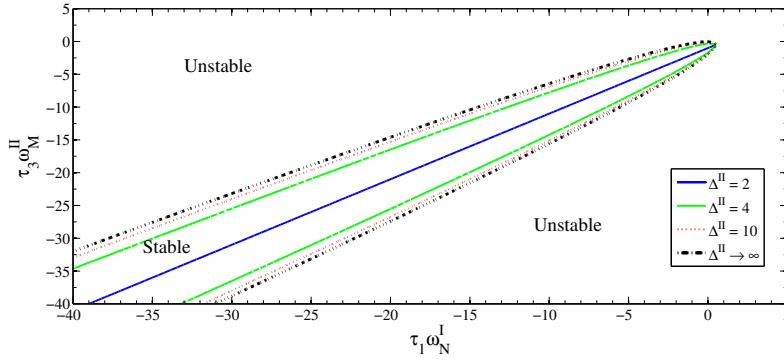

Fig. 2. Stability regions. Left: $\Delta^I = \Delta^{II} = 2$. Right: $\Delta^I = 2$ and $\Delta^{II} \to \infty$.

Figure 2 shows the stability regions for $\tau_1\omega_N^I$ and $\tau_2\omega_M^{II}$ with various Δ^{II} for which $\Delta^I = 2$ is used. When $\Delta^{II} = 2$, that is, when the grid is homogeneous, the stability region is simply given as a linear line shown as the blue straight line in the figure.

As the domain size ratio between Ω^I and Ω^{II} increases the stability region becomes broader. The green and red dotted lines in the figure represent the stability region for $\Delta^{II} = 4$ and $\Delta^{II} = 10$, respectively. The black solid line represents the limit of the stability region, i.e. for $\Delta^{II} \to \infty$. The limit line is given by $(\tau_1 \omega_N^I - \tau_3 \omega_M^{II})^2 + 2\tau_3 \omega_M^{II} \le 0$ and is independent of the value of Δ^{II}.

If $\tau_1 = \tau_4 = 0$, the penalty interface conditions are basically the same as the upwind methods. If $\tau_1 = \tau_2$ and $\tau_3 = \tau_4$ then the scheme does not split the flux into the positive and negative ones but uses the flux itself in the penalty terms.

It is important to consider the averaging method with the inhomogeneous grid system since it is the popular and simplest interface conditions. For the averaging method, the continuity of q at the interface is ensured. The averaging method is a special case of the penalty method. The averaging method has been effectively used in the previous work [11] for the homogeneous grid system. Since we suppose that the boundary operators $\mathcal{B}$ and the spectral vanishing-viscosity SV ensure the stability at the outer boundaries $x = x_L$, and x_R, we consider only the contributions from the interface at $x = 0$.

Now we consider the following penalty scheme for the averaging method

$$
\begin{aligned}
\frac{\partial q_N^I}{\partial t} + \frac{\partial I_N^I f(q_N^I)}{\partial x} &= \tau_1 Q_N(x)[f_x^+(q_N^I(0,t)) - f_x^+(q_M^{II}(0,t))] + \\
&\quad \tau_2 Q_N(x)[f_x^-(q_N^I(0,t)) - f_x^-(q_M^{II}(0,t))], \\
\frac{\partial q_M^{II}}{\partial t} + \frac{\partial I_M^{II} f(q_M^{II})}{\partial x} &= \tau_3 Q_M(x)[f_x^+(q_M^{II}(0,t)) - f_x^+(q_N^I(0,t))] + \\
&\quad \tau_4 Q_M(x)[f_x^-(q_M^{II}(0,t)) - f_x^-(q_N^I(0,t))],
\end{aligned}
\tag{13}
$$

where $f_x^\pm$ denotes the derivative $f^\pm$ with respective to x. The averaging method considered here is for the case that each subdomain can have different polynomial orders such as N and M for Ω^I and Ω^{II}, respectively. In [11], $N = M$ has been used for the averaging.

[Averaging, [11]] The scheme (13) is the averaging method if

$$
\tau_1 = \tau_2 = \tau_3 = \tau_4 = \tfrac{1}{2}.
\tag{14}
$$

Proof: If (14) is satisfied then (13) becomes, at $x = 0$

$$\frac{\partial q_N^I}{\partial t} = \frac{\partial q_M^{II}}{\partial t} = -\frac{\partial}{\partial x}\left(\frac{1}{2}\left(I_N^I f(q_N^I) + I_M^{II} f(q_M^{II})\right)\right). \square \qquad (15)$$

If (14) is satisfied, the scheme (13) is conservative for any N and M and Δ^I and Δ^{II}. **Proof:** By multiplying (13) by the weight vectors $\vec{\omega_N^I}$ and $\vec{\omega_M^{II}}$ and using the conditions (14) we have

$$\int_{x_L}^0 \frac{\partial q_N^I}{\partial t} dx + \int_0^{x_R} \frac{\partial q_M^{II}}{\partial t} dx = -\int_{x_L}^0 \frac{\partial f_N^I}{\partial x} dx - \int_0^{x_R} \frac{\partial f_M^{II}}{\partial x} dx$$
$$+ \frac{1}{2}[f_x(q_N^I(0,t))\frac{\Delta^I}{2}\omega_N^I - f_x(q_M^{II}(0,t))\frac{\Delta^{II}}{2}\omega_0^{II}]$$
$$+ \frac{1}{2}[f_x(q_M^{II}(0,t))\frac{\Delta^{II}}{2}\omega_0^{II} - \frac{\Delta^I}{2}f_x(q_N^I(0,t))\omega_N^I].$$

Thus ignoring the outer boundaries, the RHS of the above equation becomes

$$RHS = -f_N^I(q_N^I(0,t)) + f_N^{II}(q_M^{II}(0,t)) = 0. \qquad (16)$$

Here we used the fact that $q_N^I(0,t) = q_M^{II}(0,t)$ and $f_N^I(q_N^I(0,t)) = f_N^{II}(q_M^{II}(0,t))$ from Theorem 2.1. $\square$

The conditions of the penalty parameters obtained above are independent of the orders of each subdomain. Moreover, they are independent of the domain size as well.

With (14) the scheme (13) is not necessarily stable in general.

Proof: By taking the discrete norms, the energy of (13) $E(t) = \frac{2}{\Delta^I}\int_{x_L}^0 q^2(x,t)dx + \frac{2}{\Delta^{II}}\int_0^{x_R} q^2(x,t)dx$ becomes without the boundary terms

$$\frac{1}{2}\frac{dE(t)}{dt} = -\frac{2}{\Delta^I}(q_N^I(0,t))^T A q_N^I(0,t) + \frac{2}{\Delta^{II}}(q_M^{II}(0,t))^T A q_M^{II}(0,t)$$
$$+ (q_N^I(0,t) - q_M^{II}(0,t))\left[A q_x^I - A q_x^{II}\right]$$
$$= \left[\frac{2(\Delta^I - \Delta^{II})}{\Delta^I \Delta^{II}}\right](q_N^I(0,t))^T A^\pm q_N^I(0,t).$$

11

where we use that $q_N^I(0,t) = q_M^{II}(0,t)$ and $\tau_1 = \tau_2 = \tau_3 = \tau_4 = \frac{1}{2}$. Thus if $\Delta^I \neq \Delta^{II}$, the RHS does not necessarily non-positive. The RHS, however vanishes if $\Delta^I = \Delta^{II}$ so that $E(t) = E(0)$. □

The continuity of q at the interface is ensured by using the averaging method (13). This, however, does not necessarily imply that the first derivative is also continuous at the interface. In general the first derivative is discontinuous.

2.2 Weighted spectral penalty method

In the previous section, it has been shown that the conservative and stable penalty method can be constructed for fully inhomogeneous grids, i.e. $N \neq M$ and $\Delta^I \neq \Delta^{II}$ except the averaging method. The conditions obtained in the previous section are only *necessary* conditions. For example, the stability conditions, (7) and (8) say that the scheme (3) is stable if $\tau_1 = \tau_2 = \frac{1}{2\omega_N^I}$ and $\tau_3 = \tau_4 = -\frac{1}{2\omega_M^{II}}$. These conditions, albeit stable, can yield the nonphysical reflecting solutions at the inhomogeneous domain interfaces because the positive and negative fluxes are equally penalized as we will show in this section. In this section, the weighted spectral penalty method for the inhomogeneous grid is introduced to reduce the nonphysical modes at the domain interfaces.

With the weighted spectral penalty method, the incoming or outgoing characteristics are penalized with different weights if the inhomogeneous domain system is considered such that the incoming fluxes are penalized with the larger values of the penalty parameters than the outgoing fluxes. In the Legendre spectral penalty equation (3), the weighted spectral penalty method for Ω^I exploits

$$|\tau_2| \gg |\tau_1|,$$

and for Ω^{II}

$$|\tau_3| \gg |\tau_4|.$$

The numerical simulation results of supersonic reactive cavity flow presented in this paper show that the upwind characteristic interface conditions are not enough to ensure the smooth solutions across the interfaces. We will show in the following sections that by weighting the incoming fluxes against the outgoing fluxes, the nonphysical modes at the domain interfaces can be reduced. The weight, however, can not be arbitrarily large due to the CFL restriction. In practice, we use the fixed weight for each penalty parameter. Since the problem considered in this paper is highly non-

linear, the fixed weight for $\forall t > 0$ may not be enough to prevent the growth at the interfaces. We use the local spectral vanishing viscosity method with the weighted penalty method to prevent any growth at the interfaces.

2.2.1 Reflection coefficients of the weighted penalty interface conditions

In order to explain how the weighted spectral penalty method can reduce the non-physical reflection modes, the reflection coefficients analysis is used. Here the reflection modes are obtained due to the different resolution of each subdomain across the domain interfaces although the solution can be continuous. Consider the following simple linear hyperbolic equation

$$q_t + (Fq)_x = 0, \quad q : \mathbb{R} \times \mathbb{R} \to \mathbb{R}^2, \quad x \in \mathbb{R}, \quad t > 0, \tag{17}$$

where

$$q = \begin{pmatrix} u \\ v \end{pmatrix}, \qquad F = \begin{pmatrix} 0 & 1 \\ 1 & 0 \end{pmatrix}. \tag{18}$$

The same equation has been considered to show the reflecting modes at the domain interfaces with the spectral Galerkin method in [15]. We seek a wave solution such that

$$q(x, t) = \exp(i\omega t)\hat{q}(x), \qquad x \in [-2, 2], \quad t \geq 0. \tag{19}$$

Plugging the wave solution into (18) yields

$$\hat{q}(x) = Aq_1 \exp(-i\omega x) + Bq_2 \exp(i\omega x), \tag{20}$$

where $q_1 = (1, 1)^T$ and $q_2 = (1, -1)^T$.

Suppose that we have two subdomains $\Omega^I = [-2, 0]$, and $\Omega^{II} = [0, 2]$. Let $\mathcal{B}^\pm$ be the boundary operators at the end points, i.e. $x = -2$ and $x = 2$. And f^+ and f^- are $f^\pm = F^\pm q = S\Lambda^\pm S^{-1}q$;

$$f^+ = \frac{1}{2} \begin{pmatrix} u + v \\ u + v \end{pmatrix}, \qquad f^- = \frac{1}{2} \begin{pmatrix} -u + v \\ u - v \end{pmatrix}. \tag{21}$$

Here we assume that the boundary operator $\mathcal{B}$ is taken properly such that this treatment does not destroy the global stability and there is no reflection from the boundaries. In other words, we assume that we have the perfect and stable absorbing boundary operator at $x = \pm 2$. Plugging the wave solutions into the Legendre spectral method (3), we have the following linear system at the interface, i.e. at $x = 0$,

$$\tau_1(A^I - A^{II}) - \tau_2(B^I - B^{II}) = 0, \ \tau_3(A^{II} - A^I) - \tau_4(B^{II} - B^I) = 0,$$
$$\tau_1(A^I - A^{II}) + \tau_2(B^I - B^{II}) = 0, \ \tau_3(A^{II} - A^I) + \tau_4(B^{II} - B^I) = 0.$$

The above linear systems can be rewritten in the matrix form $\mathbf{WX} = \mathbf{ZX}$ with

$$\mathbf{X} = \begin{pmatrix} A^I \\ B^I \\ A^{II} \\ B^{II} \end{pmatrix}, \quad \mathbf{W} = \begin{pmatrix} -\tau_1 & \tau_1 & 0 & 0 \\ -\tau_2 & \tau_2 & 0 & 0 \\ 0 & 0 & -\tau_3 & \tau_3 \\ 0 & 0 & -\tau_4 & \tau_4 \end{pmatrix}, \quad \mathbf{Z} = \begin{pmatrix} 0 & 0 & -\tau_1 & \tau_1 \\ 0 & 0 & -\tau_2 & \tau_2 \\ -\tau_3 & \tau_3 & 0 & 0 \\ -\tau_4 & \tau_4 & 0 & 0 \end{pmatrix}.$$

The system is not well-posed as $\det(\mathbf{W} - \mathbf{Z}) = 0$. In fact this linear system can be solved by taking into account that A^{II} and B^{II} are considered as the given boundary values for the solution of Ω^I and A^I and B^I of Ω^{II} in the real computation. In order to look at the possible reflecting modes at the interface, assume that the non-zero wave solutions are locally defined only in Ω^I, that is, the solution is compactly supported in Ω^I such that it vanishes in Ω^{II}. Thus $A^{II} = B^{II} = 0$. We take the ratio of the coefficients at the interface using

$$\tau_1 A^I - \tau_2 B^I = 0, \qquad \tau_1 A^I + \tau_2 B^I = 0.$$

Define the reflection coefficients R_0 at $x = 0$ for Ω^I. Since A is corresponding to the outgoing flux and B to the incoming flux at $x = 0$, respectively, the reflection coefficients R_0 is given by

$$R_0 = \left| \frac{B^I}{A^I} \right| = \left| \frac{\tau_1}{\tau_2} \right|. \tag{22}$$

Table I
Interface conditions and reflection coefficients.

Case	Interface conditions	Reflection coefficients
T-1	$\tau_1 = 0$	$R_0 = 0$
T-2	$\tau_1 = \tau_2 = \tau$	$R_0 = 1$
T-3	$\tau_1 \ll \tau_2$	$R_0 \ll 1$
T-4	$\tau_1 \gg \tau_2$	$R_0 \gg 1$

We shall consider four different cases as given in table I. By definition, there is no reflection at the interface for the case T-1, the upwind method. For the case T-2, we do not split the flux

$$\tau_1 f^+ + \tau_2 f^- = \tau(f^+ + f^-) = \tau f. \tag{23}$$

14

Consequently, the reflection is obvious although the method is simple. The case T-3 is the weighted penalty method. The case T-4 weights the outgoing flux against the incoming flux.

For illustration, consider a step function, i.e.

$$u = v = \begin{cases} 1 & x \in \Omega^I \\ 0 & x \in \Omega^{II} \end{cases}.$$

Figure 3 shows the solutions after one time integration at $t = \Delta t = 0.0001$ for each case in Table 1. $\tau_1 = \tau_2 = \frac{1}{2\omega_N}$ are used for the case T-2, $\tau_2 \sim \mathcal{O}(N^3)$ and $\tau_1 \sim \mathcal{O}(N^2)$ are used for the case T-3 and $\tau_1 \sim \mathcal{O}(N^3)$ and $\tau_2 \sim \mathcal{O}(N^2)$ are used for the case T-4. Note the different behaviors of the case T-3 and the case T-4. For the case T-3 the penalty parameters associated with the incoming flux are weighted while the outgoing flux are weighted for the case T-4. The solution for the case T-3 does not show the overshoot at the interface for Ω^I. For the case T-4, the solution of Ω^I at interface shows the overshoot. The behaviors of the interface solution of Ω^{II} for each case can be explained by taking into account that the scheme is in fact conservative.

(a) T-1: $\tau_1 = 0$ (b) T-2: $\tau_1 = \tau_2 = \frac{1}{2\omega_N}$

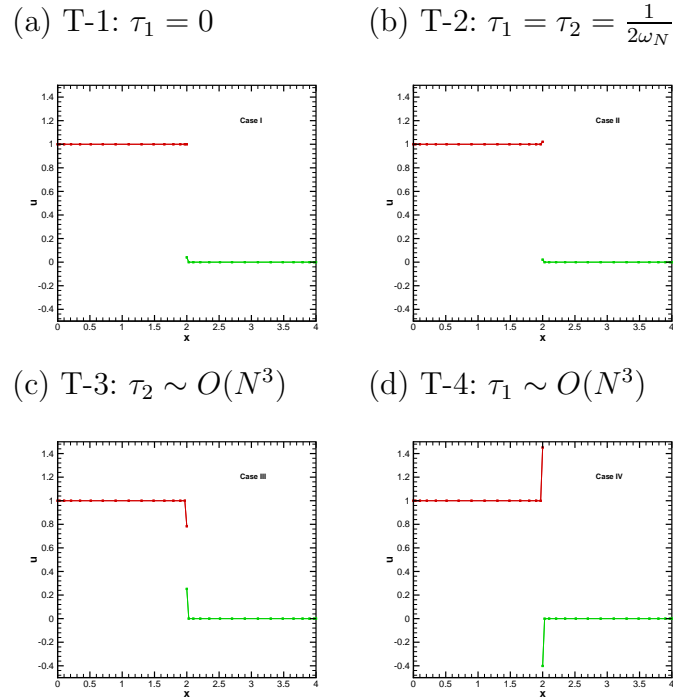(c) T-3: $\tau_2 \sim O(N^3)$ (d) T-4: $\tau_1 \sim O(N^3)$

Fig. 3. *Shock calculation at the first time step*

2.2.2 Reflection and instability

We consider more numerical examples to confirm the performance of the weighted spectral penalty method.

Homogeneous grid: First consider the same wave equation with the boundary conditions

$$q = (u,v)^T, \quad f = Fq = (v,u)^T, \tag{24}$$

$$Bq := \begin{cases} u(x,t) - v(x,t) = 0, & x = 4 \\ u(x,t) + v(x,t) = 0, & x = 0 \end{cases}, \tag{25}$$

where $\mathcal{B}$ is the boundary operator. Here we again consider two subdomains $\Omega^I = [0,2]$ and $\Omega^{II} = [2,4]$ with the same polynomial order N. For the boundary conditions at $x = 0$ and $x = 4$, we use the non-reflecting boundary conditions. The spectral penalty method (3) described in the above sections is used with the Legendre polynomials.

We denote M-A, M-UW, M-NFS and M-WP by the averaging, upwind, no-flux splitting and the weighted penalty methods, respectively. They are listed in the following table below.

Method	Interface Conditions		Remark
M-A	$\tau_1 = \tau_2 = \tau_3 = \tau_4 = \frac{1}{2}$		Averaging Method
M-UW	$\tau_1 = \tau_4 = 0, \tau_2 = -\tau_3 = \frac{1}{\omega_N}$		Upwind Method
M-NFS	$\tau_1 = \tau_2 = -\tau_3 = -\tau_4 = \frac{1}{2\omega_N}$		No-flux-Splitting Method
M-WP	$O(\tau_2) = O(\tau_3) \sim N^3, \tau_1 \neq 0 \neq \tau_4$		Weighted Penalty Method

Note that all four methods satisfy the stability condition derived in (8) as each subdomain has the same polynomial order N and domain length Δ.

The CFL condition is given by

$$\min_i \frac{\Delta t}{\Delta x_i} \leq C_{FL}, \tag{26}$$

where C_{FL} is a positive constant and taken to make Δt is small enough for every case.

Table II

The maximum error (L_∞) for M-A, M-UW, M-NFS and M-WP at time $t = 1.5$.

N\Method	M-A	M-UW	M-NFS	M-WP
4	0.67	0.82	0.13E+01	0.74
8	0.65E-02	0.28E-02	0.82E-02	0.57E-02
16	0.34E-09	0.38E-09	0.65E-09	0.29E-09
32	0.52E-11	0.52E-11	0.52E-11	0.52E-11
64	0.54E-11	0.51E-11	0.54E-11	0.50E-11

Table II shows the L_∞ error for each method. The overall performance is almost the same for each method while the M-WP performs slightly better than the other methods.

Inhomogeneous grid

Now we consider the same problem with 3 subdomains, each of them having the same domain intervals, i.e. $\Omega^1 = [0, 2], \Omega^2 = [2, 4]$ and $\Omega^3 = [4, 6]$. For these three subdomains, consider the following two different cases:

Case	Grid resolution
C-1 (homogeneous)	$N_1 = N_2 = N_3 = 8$
C-2 (inhomogeneous)	$N_1 = 8, N_2 = 32, N_3 = 8$

Note that every method satisfies the stability condition for the case C-1. For the case C-2, only the M-A, which is the averaging method, does not satisfy the stability condition as explained in Section 2.1, but the M-NFS still satisfies the stability condition.

Table III shows the L_∞ error for each case for the whole domain. As shown in the table, the M-A and the M-NFS show the instability at the interfaces for the case C-2. Table IV shows the L_∞ error for Ω^2 for each case. The L_∞ error for Ω^2 is less than that of global L_∞ error for the M-UW and the M-WP of the case C-2 because the higher polynomial order of N is used.

17

Table III
The maximum error (L_∞) for the case C-1 and the case C-2 at time $t = 1.5$.

Case\Method	M-A	M-UW	M-NFS	M-WP
C-1	0.83E-02	0.29E-02	0.11E-01	0.52E-02
C-2	unstable	0.25E-02	unstable	0.65E-02

Table IV
The maximum error (L_∞) of Ω^2 for C-1 and C-2 at time $t = 1.5$.

Case\Method	M-A	M-UW	M-NFS	M-WP
C-1	0.83E-02	0.29E-02	0.10E-01	0.51E-02
C-2	unstable	0.13E-02	unstable	0.51E-02

The instabilities of the M-A and the M-NFS are illustrated in Fig. 4. In the figure, the top figures represent the M-A at $t = 0.4$ and the bottom figures the M-NFS at $t = 1.5$. The left figures show $u+v$ and the right $u-v$. As shown in the figures, the locations of the instability are different for the M-A and the M-NFS. Since $N_2 > N_1 = N_3$, there exist higher modes in Ω^2 which do not appear in the approximations for both Ω^1 and Ω^3. For the M-A, i.e. the averaging method, the figure indicates that the instability occurs at the interface of Ω^1 and Ω^2 for $u + v$, and the instability at the interface of Ω^2 and Ω^3 for $u-v$. This implies that the sudden growth at the interface occurs when the characteristic of the lower modes enters the subdomain where the higher modes appear in the approximation. For the M-NFS, the growth occurs at different locations. If the outgoing characteristic is approximated with the higher modes, such modes in the approximation are reflected as if the adjacent subdomain plays a role as a wall boundary. The subdomain Ω^2 yields a free boundary condition for the lower mode wave solutions entering Ω^2. No significant growth at the interface is not observed for the weighted penalty method.

2.2.3 Adaptive super-viscosity method

As mentioned above, we use the fixed weight for each penalty parameter for the real computation and this is not enough for preventing the growth at the interface if the grid system is highly inhomogeneous. The super-viscosity method is used at the interface when the weighted penalty method fails to reduce the nonphysical growing modes. The super-viscosity method is only applied when and where it is necessary. Since the nonphysical reflecting or growing modes are mainly contained in the higher modes, the super-viscosity can be used to remove such higher modes locally at the interface. This technique is critical for the stabilization of the multi-domain spectral

(a) M-A, (u+v)   (b) M-A, (u-v)
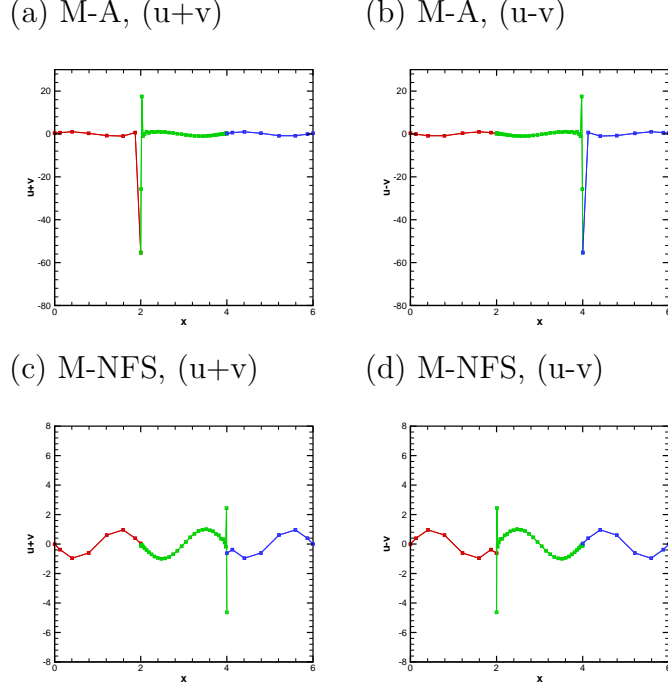

(c) M-NFS, (u+v)   (d) M-NFS, (u-v)

Fig. 4. Solutions for the M-A at time $t = 0.4$ and the M-NFS at time $t = 1.5$. The $u + v$ and $u - v$ characteristic waves are shown in the left and right columns, respectively.

penalty method for the nonlinear problems.

For the numerical experiment, we revisit the simple wave problem used in [5],

$$
\begin{cases}
\frac{\partial u}{\partial t} + \frac{\partial u}{\partial x} = 0 & x \in \Omega = (a, b), \quad t > 0 \\
u(a, t) = u_L(t) & t > 0 \\
u(x, 0) = \cos(\pi x) & x \in \Omega
\end{cases}
\tag{27}
$$

We seek an approximation of u with two subdomains, $\Omega^1 = [0, 2]$ and $\Omega^2 = [2, 4]$ with $N_1 \neq N_2$.

Two cases of grid resolution N in each subdomain are examined for the M-A and the M-NFS :

Case	Grid resolution
C-3	$N_1 = 32, N_2 = 8$
C-4	$N_1 = 8, N_2 = 32$

19

Table V shows the L_∞ errors of the case C-3 and the C-4. The table shows that the methods are stable in either case except the M-A and the M-NFS. Both of them are unstable if $N_1 < N_2$ and $N_2 < N_1$, respectively.

Table V
The maximum error (L_∞) for C-3 and C-4 at time $t = 1.5$.

Case/Method	M-A	M-UW	M-NFS	M-WP
C-3	0.13E-01	0.46E-02	4.89 (Unstable)	0.49E-02
C-4	0.54E+17 (Unstable)	0.46E-02	0.461E-02	0.46E-02

To avoid the growth in time the artificial super vanishing viscosity(SV) term is added at the interface:

$$\frac{\partial u_N}{\partial t} + \frac{\partial u_N}{\partial x} = \frac{1}{N^{2s-1}} \left[\frac{\partial}{\partial x}(1 - x^2)\frac{\partial}{\partial x} \right]^s u_N + PT \qquad x \in \partial\Omega \qquad (28)$$

where s is a positive integer growing with N [16,20] and PT denotes the penalty term. This SV method is equivalent to the filtering method [16,20]. The exponential filter method with the filtering order γ is used for the numerical experiment. The exponential filter function $\sigma(k)$ and the filtering order γ are defined as $\sigma(k) = \exp(-\epsilon_M(k/N)^\gamma)$ where k is the mode number $k = 0, \cdots, N$ and N is the polynomial order used. The positive constant ϵ_M is chosen such that $\sigma(N)$ becomes machine zero. Typically $\epsilon_M \sim 32$.

Table VI shows the results for the M-A and the M-NFS with the different orders of filtering γ. As the table indicates there no significant growth has been observed. Comparing with the results in Table II, however, we notice that the filtering method permits a lose of accuracy. For example, the L_∞ error of M-NFS/C-3($N = (32,8)$) is 0.11×10^{-1} and M-NFS/C-4 ($N = (8,32)$) is 0.46×10^{-2}. Table VI also indicates that the methods are stable even though $\gamma \to \infty$, which implies that stability can be achieved even with the small viscosity added.

Fixing the filtering order $\gamma = 16$, Table VII shows the full recovery of the accuracy as N increases.

Here we note that the weighted penalty method is proposed for the 1D. For the 2D problem, one needs to find the proper conditions for the corner of each subdomain. Such conditions will be investigated in our future work. The 2D numerical experiments indicate, however, that the proposed method with the SV method applied at the interface and corner yields a stable and accurate result as shown in the next sections.

Table VI
The maximum error (L_∞) for the reconstruction method.

	(M-A/C-4) (Ω^1)	(M-NFS/C-3) (Ω^2)
$\gamma = 2$	1.13	0.18
$\gamma = 4$	0.66	0.11E-01
$\gamma = 8$	0.21	0.11E-01
$\gamma = 16$	0.76E-01	0.11E-01
$\gamma = 16^3$	0.15E-01	0.11E-01

Table VII
The maximum error (L_∞) for the reconstruction method ; $\gamma = 16$.

	(M-A/C-4) (Ω^1)	(M-NFS/C-3) (Ω^1)
$N = 4$	1.24	1.00
$N = 8$	0.76E-01	0.11E-01
$N = 16$	0.47E-06	0.12E-08
$N = 32$	0.74E-11	0.52E-11

3 Injector-cavity scramjet system

In this section, the proposed weighted spectral penalty method is applied for the approximation of the supersonic flow interactions for the cavity-injector system with the inhomogeneous grid system. To refine the localized injector field, we use the narrow subdomain for the injector. The polynomial order of each domain is the same for both $x-$ and $y-$ directions. Thus the grid inhomogeneity in this case comes from the different domain length.

3.1 The cavity system and the governing equations

Cavity has been actively used as a flame-holder in scramjet engine (see the review by Ben-Yakar and Hanson [4]). The injector-cavity system is illustrated in Figure 1. The cavity system is categorized into 4 different types such as open, closed, transitional-closed and transitional-open depending on the length scale of cavity [4]. The cavity system with the length-to-depth ratio $L/D < 7 \sim 10$ is called an open cavity as the upper shear layer reattaches itself at the back face. Under the shear layer formed

21

over cavity, the flows with the hydrogen fuel are possibly captured inside cavity and generate the recirculation zone. The generated recirculation interacts with the shear layer and the acoustic waves inside cavity. The radicals from the chemical reaction between the hydrogen and oxygen gases reside inside cavity and trigger the auto-ignition of the supersonic engine. In principle, the more stable and longer recirculation is maintained, the more efficient fuel performance can be achieved.

The major question of the cavity flame-holder system that needs to be investigated is: *How does the fuel injection interact with cavity flows?* There have been many numerical studies on the recirculation and stabilizations of the flow inside cavity but rarely on how the continuous supply of the fuel can affect the flow dynamics inside cavity [2,3,7,21,22,25,26]. Since the injection of the fuel in the combustor is necessary, however, the injection emerges as another important key parameter for the optimal configuration of the cavity flame-holders. Both comprehensive laboratory and numerical experiments have to be carried out to answer the question. In this work, we use the length-to-depth ratio $L/D = 4\text{cm}/1\text{cm} = 4$, that is, we use the open cavity.

The governing equations are the compressible 2D reactive Navier-Stokes equations with the chemical source terms given by

$$\frac{\partial q}{\partial t} + \frac{\partial F}{\partial x} + \frac{\partial G}{\partial y} = \frac{\partial F_\nu}{\partial x} + \frac{\partial G_\nu}{\partial y} + C, \tag{29}$$

where $q = (\rho, \rho u, \rho v, E, \rho\mathbf{f})^T$ is the state vector, $F = (\rho u, \rho u^2 + P, \rho uv, (E+P)u, \rho\mathbf{f}u)^T$ and $G = (\rho v, \rho uv, \rho v^2 + P, (E+P)v, \rho\mathbf{f}v)^T$ the inviscid fluxes, F_ν and G_ν the viscous fluxes and C the chemical source term, respectively. Here ρ, u, v, E, P, and $\mathbf{f}$ denote the density, the velocity in x-direction and the velocity in y-direction, the total energy, the pressure and the mass fraction vector, respectively. The chemical model uses four chemical species, H_2, O_2, H_2O and N_2 with the reversible chemical reaction between hydrogen and oxygen gases given by

$$2H_2 + O_2 \rightleftharpoons 2H_2O. \tag{30}$$

A modified Arrhenius law gives the equilibrium reaction rate k_e, the forward reaction rate k_f and the backward reaction rate k_b as

$$
\begin{aligned}
k_e &= A_e T \exp(4.60517(E_e/T - 2.915)), \\
k_f &= A_f \exp(-E_f/(RT)), \\
k_b &= k_f/k_e,
\end{aligned}
$$

where $E_e = 12925$, and $E_f = 7200$ are the activation energy and $A_e = 83.006156$, and

$A_f = 5.541 \times 10^{14}$ are the frequency factors. R is the universal gas constant. Each chemical species has different dynamical viscosity μ_i based on the Sutherland's law. The mixture viscosity μ is obtained according to the Wilke's law [24]. The Prandtl number Pr and the Schmidt number Sc are taken to be 0.72 and 0.22 respectively for the normal air. The equation of state is given by the assumption of the perfect gas law. Detailed formulation of the equations can be found in [9,11].

With L fixed we consider four different angles of the aft wall, i.e. 90° and 30°. For the fluid conditions, the free stream Mach number $M = 1.91$, total pressure $P = 2.82$atm, total temperature $T = 830.6$K and normalized Reynolds number $R_e = 3.9 \times 10^7 \mathrm{m}^{-1}$. Note that the Reynolds number is normalized and has the unit of $1/[length]$, and that the Reynolds number based on the cavity dimensions is about $O(10^5)$. The boundary layer thickness scale is $\delta = 5 \times 10^{-4}$m, and the wall temperature is $T_w = 460.7835$K. For more detailed physical configuration and its explanation, we refer [11]. The hydrogen fuel is injected 1.5cm ahead of the cavity with the injection Mach number $M = 1$ (see Figure 1). The numerical experiments are conducted with two different sizes of the injector diameter, $d = 2$mm and $d = 2$cm to investigate the effect of the injector-channel flow interactions on the development of the shear layer over cavity. The fuel is injected into the channel flow with the direction normal to the base wall. The total pressure and the total temperature of the hydrogen jet are 2.828522atm and 830.6K respectively.

3.2   Grid inhomogeneity and the weighted penalty method

To deal with the grid inhomogeneity we use the weighted penalty method described in Section 3.

The weighted penalty method is based on the characteristic decomposition and it does not modify the stability conditions associated with $\mathbf{A}_\nu \cdot \mathbf{q}$ and $\mathbf{A}_\nu \cdot \partial \mathbf{q}$ for the Navier-Stokes equations in [11].

Figure 5 shows the effect of the grid inhomogeneity on the solution. The subdomain containing the injector has a smaller domain length than the channel subdomains. The left figure shows the solution based on the averaging method (M-A) and the right shows the solution based on the weighted penalty method (M-WP). The figures clearly show that the averaging interface condition (M-A) yields a nonphysical concentration near the domain interface while the weighted penalty interface condition (M-WP)

yields smooth solutions across the interfaces. Figure 6 shows the results near the injector subdomain with the weighted penalty method. The figure shows the flow streamline near the injector. The figures show that there is no significant reflection at the injector subdomain interfaces. It is also shown that the flow fields are well resolved with the weighted penalty method. The small recirculation formed in front of the injector is clearly seen. Such recirculation is physically formed due to the interaction between the incoming channel flow and the hydrogen jet with the no-slip boundary condition at the wall [3,4].
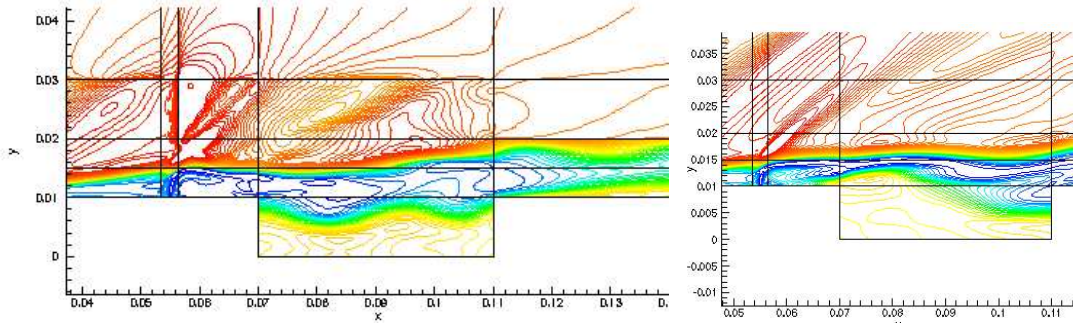
Fig. 5. Density contour of injector-cavity-channel flow by reactive Navier-Stokes equations for the normal cavity flame-holder. Each subdomain has the same polynomial order for the approximation, that is, each subdomain has N grid points both in $x-$ and $y-$directions but the different subdomain length. The left figure shows the solution using the averaging interface conditions (M-A) and the right figure shows the solution using the weighted penalty interface conditions (M-WP). The weighted penalty interface condition method considerably reduces the nonphysical density concentration near the interfaces seen in the left figure.
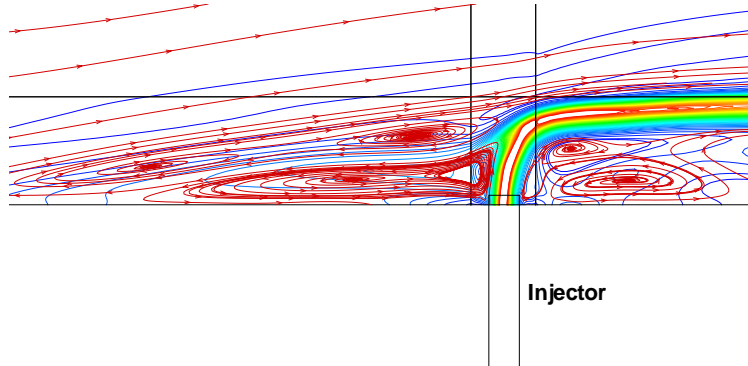
Fig. 6. The recirculation zones formed in front of the hydrogen jet: the flow streamlines are given with the hydrogen jet contour for the narrow injector-cavity system at $t = 0.225$ms.

24

3.3 Shear layer interactions

One of the major effects on the stability of the recirculation zone is by the shear layer over cavity. In [4] (also see references therein), several effects on the shear layer formation and its interaction with the cavity have been discussed including the location, size and the total number of injectors. For the numerical experiments, we consider two different injectors, the narrow and broad injectors. Figure 7 shows the water contours for both cases. By placing the injector ahead of the cavity front wall, the pressure fluctuations are reduced and the sharp gradients found near the corner of the aft wall are also weakened as the shear layer is being developed. The figures show that the broader injector has more enhanced shear layer growth over the cavity than the narrow jet. However, the pressure profiles in Figures 9 and **??** indicate that the pressure oscillations can be more attenuated with the narrow injector than the broad injector. This implies that there exists an optimal size of the injector with the fixed location of the injector from the front cavity wall that minimizes the pressure fluctuations and maximizes the stability of the recirculation zones inside cavity. Both the broad and narrow injector systems also show that they have weaker flow gradients near the aft wall than the flow gradients obtained in our previous work without the injector. The injection angle is normal to the wall but different injection angles can be used. In [3,4], it has been discussed that the angled injector such as $30°$ or $60°$ can further weaken the possible bow shock found at the aft wall. Figure 8 shows some detailed differences of the water and hydrogen profiles between the normal and recessed cavities at $t = 3.48$ms for the narrow injector system.

3.4 Pressure fluctuations

In [11], we considered the cold and reactive flows without the hydrogen injector and showed that the pressure fluctuations inside cavity can be considerably reduced if the aft wall is slanted. Consequently this helps more stable recirculation inside cavity to be developed. The generated acoustic waves disturbing the recirculation are reflected back to the shear layer due to the slantness of the rear wall. Similar results are found in the cavity system with the injection fields. Figure 9 shows the pressure fluctuation history profiles for the normal ($90°$, top figures) and slanted wall ($30°$, bottom figures) cases for the broad (left) and narrow (right) injectors. In the figures, the pressure fluctuations are measured to $tU_o/D \sim 150$ but plotted in the same scale used in Figure 6 of [11] for the comparison. The pressures are measured at the center of cavity. For the broad injector-cavity system, it is clearly shown that
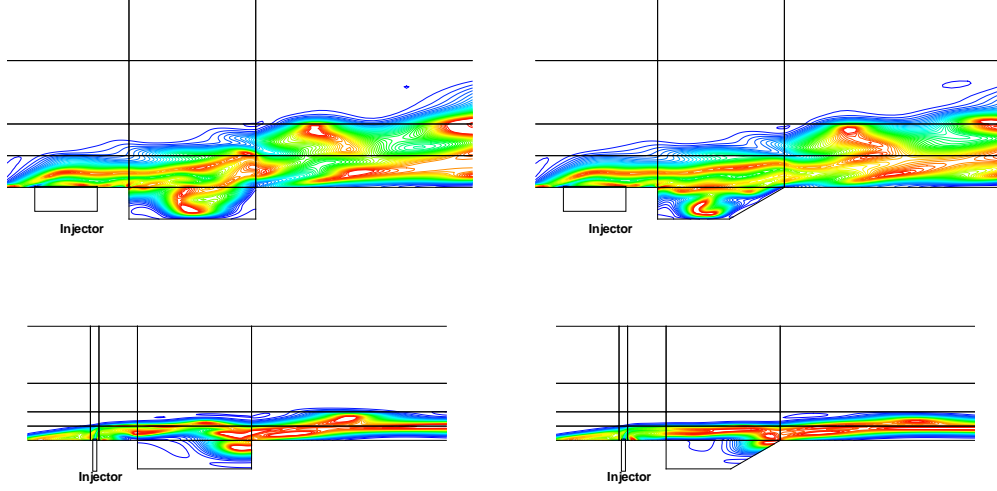
Fig. 7. Water production and transport for 90° and 30° cavity walls: the upper figures shows the broad injector-cavity system and the bottom figures the water contours of the narrow injector-cavity system at $t = 0.225$ms, respectively. There are 50 contour levels ranged from -0.001 to 0.23.
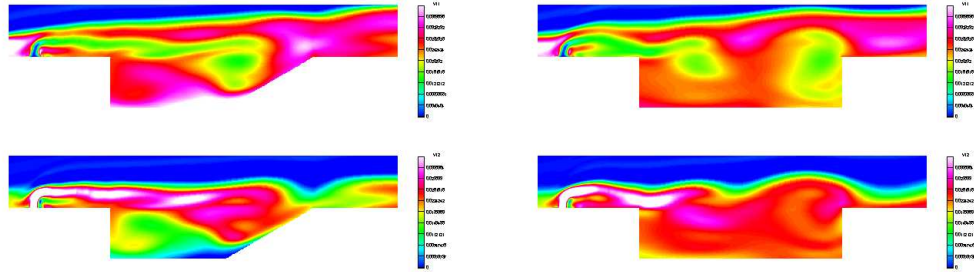

Fig. 8. Water and hydrogen density profiles at $t = 3.48$ms for the narrow injector-cavity system with 30° and 90° aft walls. The top figures show the water density contours and the bottom figures the hydrogen density contours.

the pressure fluctuations are much attenuated for the lower aft wall case and these features are similar to those for the non-reactive cold flow cases. For the narrow injector-cavity system, the pressure fluctuations for both 90° and 30° wall cavities are highly attenuated compared to those for the broad injector-cavity system. The differences of the pressure fluctuations between 30° and 90° are not significant, but one can observe that the lower angled wall cavity has less pressure fluctuations than the normal wall cavity. These results are similar to those for the reactive flow cases without the injection fields. Note that the pressure fluctuations of the normal wall cavity system are also much attenuated compared to the pressure fluctuation of the normal wall cavity system without the injection fields. The injector field in front of the cavity increases the stability of the recirculation inside cavity.
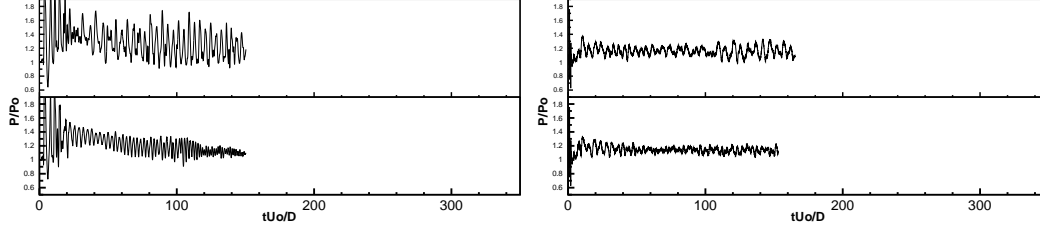
Fig. 9. Pressure history for broad (left) and narrow (right) injector-cavity flows at the center of cavity. For the broad jet, the diameter is $d = 2$cm and $d = 2mm$ for the narrow jet. Each panel shows the case of $90°$ and $30°$ cavity walls from top to bottom.

4   Summary

In this research, the direct numerical simulation of the supersonic injector-cavity scramjet system has been carried out with the multi-domain spectral penalty method with the inhomogeneous grid system. In order to minimize the development of the nonphysical modes generated at the domain interfaces due to the grid inhomogeneity, we first described the stable and conservative interface conditions of the multi-domain spectral penalty method for the inhomogeneous grid system. For general inhomogeneous grid system, it is shown that it is possible to construct a stable and conservative spectral penalty method. For the averaging method, it is also shown that the conservativity can be preserved but the stability is not maintained in general. The weighted penalty interface conditions is then proposed to minimize the non-physical effect at the inhomogeneous grid interfaces. The weighted penalty method gives more weight to the incoming fluxes than the outgoing fluxes. For the numerical experiments, we use the fixed weight for all time. The weight, however, can be adaptively determined depending on the flow conditions. Such adaptivity will be investigated in our future work. The weight penalty method reduces the nonphysical growth at the domain interface considerably but not completely. The adaptive filtering method is used with the weighted penalty method to stabilize any growth at the interface. The adaptive filtering is only applied at a small number of points at the interface. The direct numerical simulation shows that the proposed method successfully yields the stable and accurate approximation of the injector-cavity flows with the inhomogeneous grids. It is qualitatively shown that the recessed cavity yields a better performance of the pressure fluctuation reduction and enhances the stability of the recirculation zones inside cavity. The injector located in front of the cavity also reduces the pressure fluctuations inside cavity. More detailed geometric configurations maximizing the attenuation of the pressure fluctuations and the stability of the recirculation inside cavity will be investigated in our future work. The future research work will also center around the development of the 3D spectral penalty method with the weighted penalty conditions.

References

[1] R.A. Baurle and M.R. Gruber, *A study of recessed cavity flowfields for supersonic combustion applications*, AIAA-98-0938, 1998.

[2] R.A. Baurle, R.P. Fuller, J.A. White, T.H. Chen, M.R. Gruber, A.S. Nejad, *An Investigation of Advanced Fuel Injection Schemes for Scramjet Combustion*, AIAA Paper 98-0937, 1998.

[3] R. A. Ben-Yakar and R. K. Hanson, *Cavity flameholders for ignition and flame stabilization in scramjets: review and experimental study*, AIAA-98-3122, 1998.

[4] A. Ben-Yakar and R. K. Hanson, *Cavity flame-holders for ignition and flame stabilization in scramjets: an overview.*, J. Propul. Power **17** (4), 2001.

[5] C. Canuto, M.Y. Hussaini, A. Quarternoni and T. Zang, *Spectral Methods in Fluid Dynamics*, Springer-Verlag, New York, 1987.

[6] M. H. Carpenter, D. Gottlieb, C.-W. Shu, ICASE 2001-44 (2001). *On the conservation and convergence to weak solutions of global schemes*, J. Scientific Comput. **18** (1), 2003.

[7] D. L. Davis and R. D. W. Bowersox, AIAA paper 97-3274 (1997).

[8] P. J. Diamessis, J. A. Domaradzki and J. S. Hesthaven, *A spectral multidomain penalty method model for the simulation of high Reynolds number localized incompressible stratified turbulence*, J. Comput. Phys. **202**, 2005.

[9] W. S. Don and D. Gottlieb, *Spectral Simulation of Supersonic Reactive Flows*, SIAM, J. Numer. Anal. **35**, 1998.

[10] W. S. Don and D. Gottlieb, AIAA 97-0538 1997.

[11] W. S. Don, D. Gottlieb and J. H. Jung, *A multidomain spectral method for supersonic reactive flows*, J. Comput. Phys. **192** (1), 2003.

[12] W. S. Don and C. B. Quillen, *Numerical simulation of shock-cylinder interactions I : resolution*, J. Comput. Phys. **122**, 1995,

[13] D. Funaro and D. Gottlieb, *A New Method of Imposing Boundary Conditions in Pseudospectral Approximations of Hyperbolic Equations*, Math. Comp. **51**, 1998.

[14] D. Funaro and D. Gottlieb, *Convergence Results for Pseudospectral Approximations of Hyperbolic Systems by a Penalty-Type Boundary Treatment*, Math. Comp. **57**, 1991.

[15] S. Gottlieb and J.-H. Jung, *Numerical Issues in the Implementation Of High Order Polynomial Multidomain Penalty Spectral Galerkin Methods for Hyperbolic Conservation Laws*, Commun. in Comput. Phys., in press, 2008.

[16] B. Y. Guo, H. Ma and E. Tadmor, *Spectral vanishing viscosity method for nonlinear conservation laws*, SIAM J. Numer. Anal. **39** 4, 2002.

[17] J. S. Hesthaven and D. Gottlieb, *A Stable Penalty Method for the Compressible Navier Stokes Equations. I. Open Boundary Conditions*, SIAM J. Sci. Comp. **17**, 1996.

[18] J. S. Hesthaven, *A stable penalty method for the compressible Navier-Stokes equations II. One-dimensional domain decomposition schemes*, SIAM J. Sci. Comput.

17, 1997.

[19] J. S. Hesthaven, *A Stable Penalty Method for the Compressible Navier-Stokes Equations. III. Multi Dimensional Domain Decomposition Schemes*, SIAM J. Sci. Comp. **20** (1), 1999.

[20] H. Ma, *Chebyshev-Legendre Super Spectral Viscosity Method for Nonlinear Conservation Laws*, SIAM J. Numer. Anal. **35**, 1998.

[21] D. P. Rizzetta, Numerical simulation of supersonic flow over a three-dimensional cavity, *AIAA J* **26**(7), 799(1988).

[22] M. B. Tracy and E. B. Plentovich, Characterization of Cavity Flow Fields Using Pressure Data Obtained in the Langley 0.3-Meter Transonic Cryogenic Tunnel, NASA Technical Memorandum, 4436 (1993).

[23] H. Vandeven, *Family of spectral filters for discontinuous problems*, J. Sci. Comput. 6, 1991.

[24] C.R. Wilke, *A viscosity equation for gas mixtures*, J. Chem. Phys. **18**, 1950.

[25] X. Zhang and J. A. Edwards, An investigation of supersonic cavity flows driven by thick shear layers, *Aeronaut J* **94**(940), 355(1990).

[26] X. Zhang, A. Rona and J. A. Edwards, The effect of trailing edge geometry on cavity flow oscillation driven by a supersonic shear layer, *Aeronaut J.* **102**(1013), 129(1998).

5 Introduction

In this article we extend the one-dimensional Multi-Domain Hybrid Spectral-WENO Method (Hybrid) for Hyperbolic Conservation Laws [7] to two-dimensions in space and apply it to the classical Shock-Vortex interaction and Richtmyer-Meshkov instabilities problem. The general idea of the Hybrid method is to use a multi-domain framework in order to apply convenient spatial discretizations to the smooth and rough parts of the numerical solution. Shocks and high gradients are kept at WENO subdomains, while complex, but still smooth, details of the solution are treated within spectral subdomains. Numerical efficiency is increased with respect to the classical spectral and WENO methods: Postprocessing techniques of the spectral method approach of shocks [15,20] are avoided, since no Gibbs phenomenon will occur, and the expensive characteristic decompositions and projections of the WENO method are skipped at the smooth parts of the solution [2,4,6,12,13,19].

The main issues in the construction of the Hybrid method are the smoothness measurement of the solution and the subdomains types switching algorithm. In this work we employ the high order multi-resolution algorithm by Ami Harten [16] to build a lo-

cal classification of the solution into smooth and rough. Originally built to decrease the work of the fluxes computations of Conservation Laws, Harten's Algorithm proposes to use information from coarser grids when the solution is locally over-represented. We instead use the multi-resolution information to apply distinct numerical methodologies to the different structures of the solution. The main goal is to conjugate the higher efficiency of the spectral method with the shock-capturing capability of the WENO method. The multi-resolution analysis is used to trigger the switching algorithm to change the subdomains spatial discretizations if shocks start to develop at a spectral subdomain, or if the solution becomes smooth at a WENO one. Moving discontinuities are similarly treated by changing to (or maintaining as) WENO the subdomains on their paths and switching to (or maintaining as) spectral the subdomains that were left behind. These changes are performed via Lagrangian and spectral interpolations of the local solutions to the new discretizations grids. Interpolation is also used to patch the solutions at the interfaces. While a simple average is sufficient for the interfaces where the solution is smooth, using the same grid spacing at adjacent WENO subdomains is necessary for a conservative transmission of shocks [28]. Even though we do not have a theoretical proof of the conservation of the Hybrid scheme, we argue that with the conjugation of two conservative schemes with a conservative WENO interface and the high order accuracy of the conservative spectral scheme, the conservation error should be spectrally small. We have numerically demonstrated this fact in [7] through a long time time integration of the inviscid Burgers equations with correct shock speed and achieved excellent agreement with the analytical solution of the standard Riemann shock-tube problems, such as the Lax and the Sod problem of the Euler Equations.

The paper is organized as follows: Section 6 provides quick reviews on spectral and WENO methods. The Multi-Resolution analysis is discussed in details at Section 7 and the Hybrid Method is introduced at Section 8. The Switching Algorithm is presented in Section 8.3 and numerical experiments with two dimensional compressible flows are finally presented at Section 9. Concluding remarks are given in Section 4.

6 Spectral and WENO Methods

6.1 The Spectral Method

In spectral collocation methods, the function $u(x)$ is interpolated by a global Lagrangian interpolation polynomial of degree $N, l_j(x)$, at a given set of collocation points $\{x_j, j = 0, \ldots, N\}$ as

$$I_N u(x) = \sum_{j=0}^{N} u(x_j) l_j(x), \tag{31}$$

where I_N is the Interpolating operator and $l_j(x_i) = \delta_{ij}$.

The Lagrangian interpolation polynomial $l_j(x)$ can be constructed as

$$l_j(x) = \frac{q(x)}{(x - x_j) q'(x_j)}, \qquad q(x) = \prod_{j=0}^{N} (x - x_j), \tag{32}$$

and the derivative of $I_N u$ becomes

$$\frac{dI_N u(x)}{dx} = \sum_{j=0}^{N} u(x_j) \frac{dl_j(x)}{dx}. \tag{33}$$

In this study, we will employ the Chebyshev-Gauss-Lobatto quadrature points, namely,

$$x_j = \cos\left(\frac{\pi j}{N}\right), \tag{34}$$

which are the roots of $(1 - x^2) T'_N(x)$ and $T_N(x)$ is the N_th degree Chebyshev polynomial of the first kind. The Chebyshev interpolation polynomial is given by

$$l_j(x) = \frac{(-1)^{j+1}(1 - x^2) T'_N(x)}{c_j N^2 (x - x_j)}. \tag{35}$$

where $c_j = 1, j = 1, \ldots, N - 1$ and $c_0 = c_N = 2$.

The form of the differentiation matrix $\mathbf{D} = \frac{dl_j(x_i)}{dx}$ in (33) can be found in [8]. The mapping devised by Kosloff and Tal-Ezer [22] will also be employed to enhance the stability of the Chebyshev collocation scheme [5,9].

6.2 Filters

Spectral methods are highly efficient and accurate, when the solution and its derivatives are smooth. In the presence of discontinuities, however, Gibbs Phenomenon generates oscillations that contaminate the solution and causes the loss of the exponential convergence. This is explained in spectral space by the linear decay rate of the coefficients a_n of the global expansion:

$$u(x) = \sum_{n=0}^{\infty} a_n T_n(x). \tag{36}$$

In such a situation, one can modify the global expansion coefficients a_n to enhance the convergence properties of the approximation via a filter function $\sigma(\eta)$ [30] with the following properties

$$\begin{aligned}
\sigma(\eta) &= \sigma(-\eta), \quad \sigma(\pm 1) = 0, \\
\sigma(0) &= 1, \quad \sigma^{(q)}(0) = 0 \quad q = 1, \ldots, p - 1.
\end{aligned} \tag{37}$$

If $\sigma(\eta)$ has at least $p - 1$ continuous derivatives, $\sigma(\eta)$ is termed a p_th order filter. It was proved in [30] that the filtered expansion converges faster to the correct solution than the unfiltered original one in the case of a discontinuous function. Moreover, the convergence rate depends solely on the order and the compactness of the filter function $\sigma(\eta)$ and the distance from the discontinuities.

The filter function used in this study is the Exponential filter given by

$$\sigma(\eta) = \exp(-\alpha\eta^p), \tag{38}$$

where $\alpha = -\ln(\epsilon)$ and ϵ is the machine zero.

The spectral filtering can be expressed

- in the physical space as:

$$F_N u(x_i) = \sum_{j=0}^{N} u(x_j)\Phi_{ji}, \quad \Phi_{ji} = \frac{2}{Nc_j} \sum_{n=0}^{N} \frac{1}{c_n} \sigma\left(\frac{n}{N}\right) T_n(x_i) T_n(x_j), \qquad (39)$$

- in the transformed space as:

$$F_N u(x_i) = \sum_{n=0}^{N} a_n \sigma\left(\frac{n}{N}\right) T_n(x_i), \quad a_n = \frac{2}{Nc_n} \sum_{j=0}^{N} \frac{1}{c_j} u_j T_n(x_j), \qquad (40)$$

where F_N is the filtering operator.

While filtering techniques can improve the overall convergence properties of the solution away from discontinuities, the solution near the discontinuities remains poor. Post-processing of the resulting oscillatory data to recover spectrally accurate non-oscillatory results can be performed by various reconstruction techniques, such as the direct and inverse Gegenbauer reconstruction [15,20] and Padé reconstruction [25]. Reconstruction techniques are, in general, computationally costly and certain complications might arise. For instance, as the degree of the reconstructed polynomial increases, the Gegenbauer transformation matrices become ill-conditioned due to the round-off error [20]. Moreover, the extension of these reconstruction techniques to higher dimensions is not trivial.

6.3 The WENO Method

WENO schemes were designed for the numerical solution of Hyperbolic Conservation Laws in the form (for ease of presentation the discussion is based on the one-dimensional formulation)

$$\mathbf{u}_t + \mathbf{f}(\mathbf{u})_x = 0. \qquad (41)$$

The Jacobian $\frac{\partial \mathbf{f}}{\partial \mathbf{u}}$ for (41) is needed to project the system into its characteristic form and, in general, $\frac{\partial \mathbf{f}}{\partial \mathbf{u}}$ is not constant. To overcome the difficulty when computing the flux at a cell boundary $x_{i+\frac{1}{2}}$, "local freezing" of the matrix components is employed using the Roe average $\mathbf{u}_{i+\frac{1}{2}}$ [27] defined as

$$f(\mathbf{u}_{i+1}) - f(\mathbf{u}_i) = f'(\mathbf{u}_{i+\frac{1}{2}})(\mathbf{u}_{i+1} - \mathbf{u}_i). \qquad (42)$$

The numerical scheme for (41) can be written in the conservative form as

$$\frac{du_i(t)}{dt} = -\frac{1}{\Delta x}(\hat{f}_{i+\frac{1}{2}} - \hat{f}_{i-\frac{1}{2}}), \tag{43}$$

where $u_i(t)$ is the numerical approximation to the point value $u(x_i, t)$ and Δx is the uniform grid spacing. The numerical flux based on the $\{u_j, j = i - r, \dots, i + s\}$

$$\hat{f}_{i+\frac{1}{2}} = \hat{f}(u_{i-r}, \dots, u_{i+s}), \tag{44}$$

satisfies the following conditions:

- $\hat{f}$ is Lipschitz continuous in all arguments;
- $\hat{f}$ is consistent with the physical flux f, i.e. $\hat{f}(u, \dots, u) = f(u)$.

The solution to the conservative scheme (43), if converges, will converge to a weak solution. This is known as the Lax-Wendroff theorem.

The earlier works of van Leer [29], Boris and Book [1] and Harten's TVD schemes have led to the introduction of Essentially Non-Oscillatory (ENO) schemes [18], where its basic premise is that of adaptivity of the stencil, based on the local smoothness of the solution, using only a stencil free of discontinuities in the computation of flux gradients. ENO schemes have been shown to generate sharp resolutions of shocks as well as to maintain high order of accuracy in smooth regions.

An improvement of finite volume ENO – Weighted Essentially Non-Oscillatory (WENO) schemes were proposed by Liu, Osher, and Chan [23]. WENO schemes use the same idea as ENO, except that WENO uses a convex combination of all available smooth stencils to obtain higher order of accuracy than the original ENO at smooth parts of the solution. Finite Difference WENO schemes were later proposed by Jiang and Shu [19].

In all numerical examples that follows, we use the fifth order characteristic-wise WENO finite difference formulation, making use of the Roe average for the eigensystem defined above and the global Lax-Fredrichs flux splitting

$$f^{\pm} = \tfrac{1}{2}(f(u) \pm \alpha u), \tag{45}$$

where $\alpha = \max_u \max_{1 \leq i \leq N_\lambda} |\lambda_i(u)|$ and $\lambda_i(u), i = 1, \dots, N_\lambda$ are the local eigenvalues of the Jacobian $\frac{\partial \mathbf{f}}{\partial \mathbf{u}}$. The numerical flux $\hat{f}_{i+\frac{1}{2}}$ is computed by the WENO reconstruction

procedure. The interested reader is referred to [4] for details.

7 Multi-Resolution Analysis

The successful implementation of the Hybrid method depends on the ability to obtain accurate information on the smoothness of a function. In this work, we employ the Multi-Resolution (MR) algorithms by Harten [16,17] to detect the smooth and rough parts of the numerical solution. The general idea is to generate a coarser grid of averages of the point values of a function and measure the differences (MR coefficients) d_i between the interpolated values from this sub-grid and the point values themselves. A tolerance parameter ϵ_{MR} is chosen in order to classify as smooth those parts of the function that can be well interpolated by the averaged function and as rough those where the differences d_i are larger than the parameter ϵ_{MR}. We shall see that the order of interpolation is relevant and the ratio between d_i of distinct orders may also be taken as an indication of smoothness.

Let us start by showing two examples where one can notice the detection capabilities of the Multi-Resolution analysis that will be presented below. The left and right figures of Figure 10 show the piecewise analytic function

$$f(x) = \begin{cases} 10 + x^3 & -1 \le x < -0.5 \\ x^3 & -0.5 \le x < 0 \\ \sin(2\pi x) & 0 \le x \le 1 \end{cases}, \tag{46}$$

and the density (ρ) of the Mach 3 Shock-Entropy wave interaction problem [19] as computed by the classical fifth order WENO finite difference scheme, respectively.

The test function (46) has a jump discontinuity at $x = -0.5$ and a discontinuity at its first derivative at $x = 0$. One can see that at each grid point the differences d_i decay exponentially to zero inside the analytical pieces of the function when the order of interpolation increases from $n_{MR} = 3$ to $n_{MR} = 8$. At the discontinuity $x = 0.5$, the measured differences d_i are $O(1)$ and remain unchanged despite the increase of the interpolation order. Similar behavior is exhibited at the derivative discontinuity at $x = 0$ with a smaller amplitude.

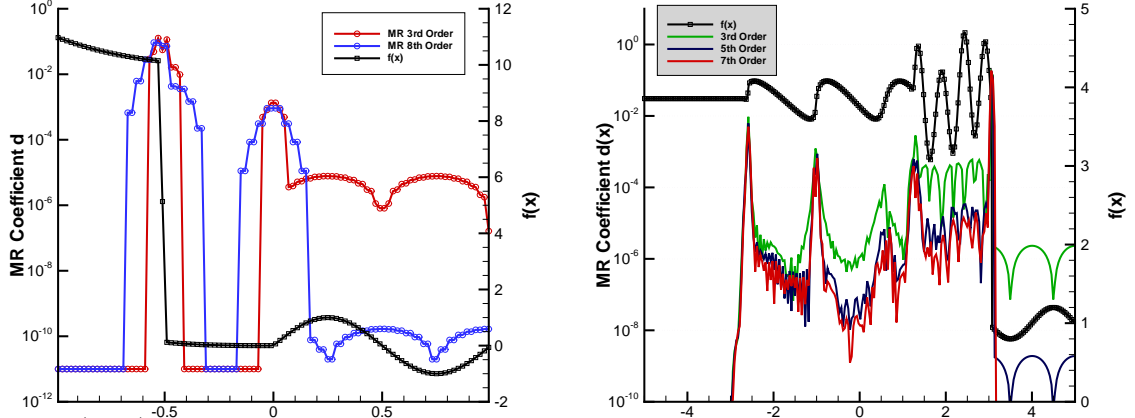Also, in the right figure of Figure 10, the density of the Mach 3 Shock-Entropy wave

Fig. 10. (Left) The third and eighth order MR coefficients d_i of the piecewise analytic function. (Right) The third, fifth and seventh order MR coefficients d_i of the density $f(x) = \rho$ of the Mach 3 Shock-Entropy wave interaction problem.

interaction problem and the corresponding MR coefficients d_i are shown for the third, fifth and seventh order Multi-Resolution analysis. The location of the main shock is at $x \approx 2.73$ and the shocklets behind the main shock are well captured. The high frequencies behind the main shock are much better distinguished with the higher orders.

Averaging a function corresponds to filter the upper half of the spectrum. The main idea of Harten's smoothness classification is to measure how distant the actual values of the function are from being predicted through interpolation of the lower half of the frequencies contained in the sub-grid of averages. We now describe a detailed construction of the sub-grid of averages and its corresponding interpolating polynomial, finishing with a worked example.

Given an initial number of grid points N_0 and grid spacing Δx_0, consider the set of nested dyadic grids $\{G^k, 0 \leq k \leq L\}$, defined as:

$$G^k = \{x_i^k, i = 0, \ldots, N_k\}, \tag{47}$$

where $x_i^k = i\Delta x_k, \Delta x_k = 2^k \Delta x_0, N_k = 2^{-k} N_0$. For each level $k > 0$ we define the set of cell averages $\{\bar{f}_i^k, i = 1, \ldots, N_k\}$ at x_i^k of a function $f(x)$:

$$\bar{f}_i^k = \frac{1}{\Delta x_k} \int_{x_{i-1}^k}^{x_i^k} f(x)dx, \tag{48}$$

and $\bar{f}_i^0 = f_i^0$. Let $\tilde{f}_{2i-1}^k$ be the approximation to $\bar{f}_{2i-1}^k$ by the unique polynomial of degree $2s$ that interpolates $\bar{f}_{i+l}^k, |l| \leq s$ at x_{i+l}^k, where $r = 2s + 1$ is the order of approximation.

36

The approximation differences, also called multiresolution coefficients, $d_i^k = \bar{f}_{2i-1}^{k-1} - \tilde{f}_{2i-1}^{k-1}$, at the k-th grid level and grid point x_i, have the property that if $f(x)$ has $p-1$ continuous derivatives and a jump discontinuity at its p-th derivative, then

$$d_i^k \approx \begin{cases} \Delta x_k^p [f_i^{(p)}] & \text{for} \quad p \leq r \\ \Delta x_k^r f_i^{(r)} & \text{for} \quad p > r \end{cases}, \tag{49}$$

where $[\cdot]$ denotes the magnitude of the jump of the function inside.

From formula (49) it follows that

$$|d_{2i}^{k-1}| \approx 2^{-\bar{p}} |d_i^k|, \qquad \text{where} \qquad \bar{p} = \min\{p, r\}. \tag{50}$$

Equation (50) shows that away from discontinuities, the MR coefficients d_i^k diminish in size with the refinement of the grid; close to discontinuities, they remain the same size, independent of k. The MR coefficients d_i^k were used in [17] in two ways. First, finer grid data $\bar{f}_i^0$ were mapped to its M level multiresolution representation $\bar{f}_i^0 = (d_i^1, \cdots, d_i^M, \bar{f}_i^M)$ to form a multiscale version of a particular scheme, where truncation of small quantities with respect to a tolerance parameter decreased the number of flux computations. Secondly, the MR coefficients d_i^k also acted as a shock detection mechanism and an adaptive method was designed where a second-order Lax-Wendroff scheme was locally switched to a first-order accurate TVD Roe scheme, whenever d_i^1 was bigger than ϵ_{MR}.

Equation (49) also indicates that the variation of the MR order, n_{MR}, can give additional information on the type of the discontinuity. Nevertheless, in this work, we will be limited at using only the first level $k = 1$ of the multiresolution coefficients and we shall drop the superscript 1 from the d_i^1 from here on unless noted otherwise.

Hence, to find d_i, the idea is to construct a piecewise polynomial $P_k(x)$ of degree $k = n_{MR}$ using $k+1$ computed average values of f_i, $\bar{f}_i$, at the equi-spaced grid x_i such that

$$P_k(x_i) = f(x_i) + O(\Delta x^{k+1}), \tag{51}$$

and

$$d_i = f_i - P_k(x_i). \tag{52}$$

Given a tolerance level ϵ_{MR}, the smoothness of the function $f(x)$ at x_i would then be

checked against the magnitude of the d_i, namely:

$$\begin{cases} |d_i| \leq \epsilon_{MR} \Rightarrow \text{solution is smooth.} \\ |d_i| > \epsilon_{MR} \Rightarrow \text{solution is non-smooth.} \end{cases} \tag{53}$$

The algorithm for computing the MR coefficients d_i is given next.

7.1 Computing the MR Coefficients

Consider an equi-spaced grid $\{x_i = i\Delta x, i = -m, \ldots, 0, \ldots, N, \ldots, N + M\}$ where Δx is the constant grid spacing. N can be an odd or an even number. Depending on N and the even or odd order of the MR Analysis n_{MR}, the number of ghost points m and M required are given in table VIII.

N	n_{MR}	m	M
odd	odd	$n_{MR} + 1$	$n_{MR} + 1$
even	odd	$n_{MR} + 1$	n_{MR}
odd	even	n_{MR}	$n_{MR} + 2$
even	even	n_{MR}	$n_{MR} + 1$

Table VIII
The number of ghost points m and M required for the MR Analysis.

Given the grid point values of the function $f(x)$, the average values are computed as

$$\bar{f}_i = \tfrac{1}{2}\left(f_{2i} + f_{2i+1}\right), \quad i = -\frac{m}{2}, \ldots, \frac{N + M - 1}{2}. \tag{54}$$

We construct a piecewise $k = n_{MR}$ degree polynomial $P_k(x)$ using the $k+1$ computed average values of the given function, $\bar{f}_i$ such that

$$P_k(x_i) = f(x_i) + O(\Delta x^{k+1}). \tag{55}$$

The polynomial $P_k(x_i)$, $l = \tfrac{1}{2}m$ and $L = l-1$ or $L = l$ if k is odd or even, respectively, can be written as

$$P_k(x_i) = \sum_{r=i-l}^{i+L} \alpha_r \bar{f}_r. \tag{56}$$

However, since the coefficients α depend only on x_i and do not depend on the function $f(x)$, the $P_k(x_i)$ can be written as:

$$P_k(x_i) = \begin{cases} \sum_{r=-l}^{L} \alpha_r \bar{f}_{i+r}, & \mod(i,2) = 0 \\ \sum_{r=-l}^{L} \beta_{r+1} \bar{f}_{i+r}, & \mod(i,2) = 1 \end{cases}. \tag{57}$$

In the case of $\mod(i,2) = 1$,

$$\beta_{-r} = \alpha_r, \quad r = -l, \ldots, L. \tag{58}$$

Furthermore, if n_{MR} is even, the coefficients α are symmetric about $r = 0$, namely, $\alpha_{-r} = \alpha_r, r = 1, \ldots, L$.

The desired coefficients α are computed by requiring $P_k(x)$ to be equal to each of the first $k+1$ monomials $f(x) = 1, x, x^2, \ldots, x^k$ and evaluated at any grid point $x = x^*$. For simplicity, we take $x^* = 0$. The $\bar{f}_i$ are evaluated for $i = -l, \ldots, L$. This procedure results in a system of linear equations, $\mathbf{A}\vec{\alpha} = \vec{b}$, where

$$\mathbf{A} = \begin{pmatrix} 1 & \cdots & 1 \\ -2l + (-2l+1) & \cdots & 2L + (2L+1) \\ \vdots & \vdots & \vdots \\ (-2l)^k + (-2l+1)^k & \cdots & (2L)^k + (2L+1)^k \end{pmatrix}, \vec{\alpha} = \begin{pmatrix} \alpha_{-l} \\ \alpha_{-l+1} \\ \vdots \\ \alpha_L \end{pmatrix}, \vec{b} = \begin{pmatrix} 1 \\ 0 \\ \vdots \\ 0 \end{pmatrix}, \tag{59}$$

and $\mathbf{A}$ is a matrix of size $(L+l+1) \times (L+l+1)$.

Using (57), the k-th order Multi-Resolution coefficients d_i at x_i can be computed as

$$d_i = f_i - P_k(x_i) \quad i = 0, \ldots, N. \tag{60}$$

One can also evaluate the α by matching the terms in the Taylor series expansion using (55) and (56) to any desired order, however this procedure may become cumbersome for high order k.

39

Example

To illustrate the procedure above, we will construct two unique local polynomials with $k = n_{MR} = 3$, such that $P_k(x_0) = f(x_0) + O(\Delta x^{k+1})$ and $P_k(x_1) = f(x_1) + O(\Delta x^{k+1})$.

To construct the desired polynomials one needs to find the unique coefficients $\{\alpha_{-2}, \alpha_{-1}, \alpha_0, \alpha_1\}$ and $\{\beta_{-1}, \beta_0, \beta_1, \beta_2\}$ such that

$$\alpha_{-2}\bar{f}_{-2} + \alpha_{-1}\bar{f}_{-1} + \alpha_0\bar{f}_0 + \alpha_1\bar{f}_1 = f(x_0) + O(\Delta x^4) \tag{61}$$

and

$$\beta_{-1}\bar{f}_{-1} + \beta_0\bar{f}_0 + \beta_1\bar{f}_1 + \beta_2\bar{f}_2 = f(x_1) + O(\Delta x^4). \tag{62}$$

The system of equations, (59), becomes

$$\mathbf{A} = \begin{pmatrix} 1 & 1 & 1 & 1 \\ -7 & -3 & 1 & 5 \\ 25 & 5 & 1 & 13 \\ -91 & -9 & 1 & 35 \end{pmatrix}, \quad \overrightarrow{\alpha} = \begin{pmatrix} \alpha_{-2} \\ \alpha_{-1} \\ \alpha_0 \\ \alpha_1 \end{pmatrix}, \quad \overrightarrow{b} = \begin{pmatrix} 1 \\ 0 \\ 0 \\ 0 \end{pmatrix}. \tag{63}$$

Solving this system yields

$$\alpha_{-2} = -\frac{3}{64}, \quad \alpha_{-1} = \frac{17}{64}, \quad \alpha_0 = \frac{55}{64}, \quad \alpha_1 = -\frac{5}{64}, \tag{64}$$

and $\{\beta_{-1} = \alpha_1, \beta_0 = \alpha_0, \beta_1 = \alpha_{-1}, \beta_2 = \alpha_{-2}\}$.

The tolerance parameter ϵ_{MR} determines the dynamic activation of the spectral and WENO spatial discretizations along the various subdomains of the hybrid method. While a too small value of ϵ_{MR} activates the more expensive WENO method at subdomains where the solution is smooth, a larger value activates the spectral method at a subdomain with low spatial resolution, generating oscillations. ϵ_{MR} also bears a straight relation with the interpolation order n_{MR}. High n_{MR} values decrease the size of ϵ_{MR} one needs to chose, since high frequencies are less mistaken by gradient jumps. The general guideline is to start with a value for n_{MR} at least equal to the order of the WENO method and increase it according to the complexity of the solution. For instance, $n_{MR} = 5$ is a good choice for the piecewise smooth solution of the SOD problem, the Entropy problem would work better with $n_{MR} = 7$. For most of the flows with shock that were tested, the value of $\epsilon_{MR} = 10^{-3}$ yielded a good balance between computational speed and accuracy of the numerical solution.
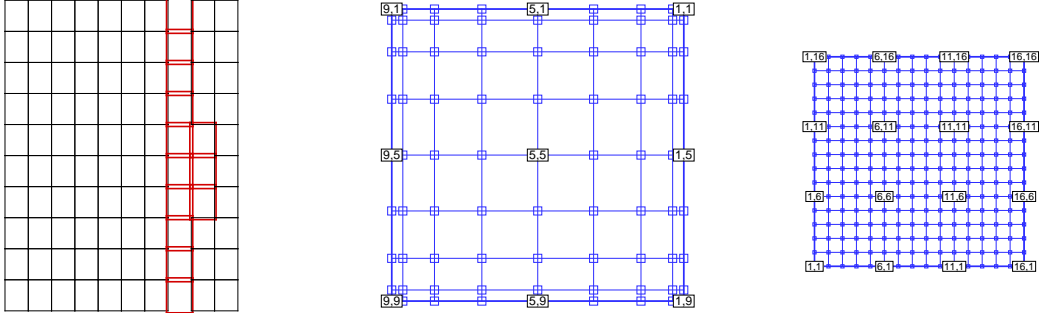
Fig. 11. (Left) Partition of the physical domain into spectral and WENO subdomains. (Middle) Typical spectral subdomain. (Right) Typical WENO subdomain.

8 The Multi-Domain Hybrid Spectral-WENO method

We now describe the implementation of the Multi-Domain Hybrid Spectral-WENO method (Hybrid), detailing the structure of the two-dimensional grid of subdomains, the interfaces treatment and the algorithm that switches the spatial discretization of the subdomains.

The main idea of the Hybrid method can be formulated as:
Avoid Gibbs phenomenon by keeping discontinuities at WENO subdomains and increase the numerical efficiency by treating the smooth parts of the solution using a spectral spatial discretization.

In this study, the physical domain is restricted to rectangular shapes and will be partitioned into a $(N_d^x \times N_d^y)$ grid of subdomains. Figure 11 shows an example of such a domain partition along with typical spectral and WENO subdomains. Note that patching of subdomains occurs due to the ghost points of the WENO discretization.

We shall use a vector $\mathbf{k} = (k_x, k_y), k_x = 1, \ldots, N_d^x, k_y = 1, \ldots, N_d^y$ to denote the coordinates of the two dimensional subdomain grid. For example, $\mathbf{k} = (2, 3)$ means the subdomain number $k_x = 2$ in the x direction and $k_y = 3$ in the y direction. Each subdomain is initialized either as a spectral or WENO subdomain. The Chebyshev-Gauss-Lobatto points are used for the spectral discretization and an uniformly spaced grid with ghost points is used as the WENO grid.

For the sake of simplicity, we consider only square subdomains, with $N_s \times N_s$ grid points at a pectral subdomain and $N_W \times N_W$ equi-spaced points at a WENO subdo-
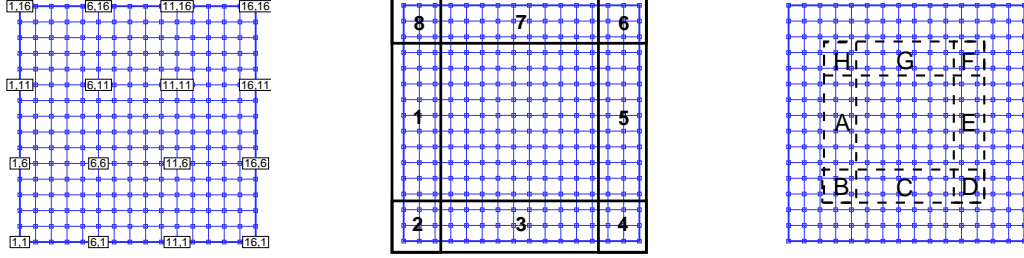
41

Fig. 12. (Left) Typical WENO subdomain. (Middle) "Ghost Area". (Right) "Buffer Area".

main. The number of ghost points is denoted by r and N_B is the number of points used for the buffer zone (see below).

8.1 Description of WENO subdomains

Each WENO subdomain $\mathbf{k}$ is composed of three parts: The "Ghost Area", the "Buffer Area", and the "Interior Area" as shown in Figure 12.

- **Ghost Area:**
  The "Ghost Area" is used for the WENO Reconstruction and for communication with its neighboring subdomains and is subdivided into eight "Ghost Zones" $\{G_i^{\mathbf{k}}, \quad i = 1, \ldots, 8\}$ (see the middle figure of Figure 12),

$$
\begin{cases}
G_8^{\mathbf{k}} = I_0^g \times J_2^g \ , \ G_7^{\mathbf{k}} = I_1^g \times J_2^g \ , \ G_6^{\mathbf{k}} = I_2^g \times J_2^g \\
G_1^{\mathbf{k}} = I_0^g \times J_1^g \ , \qquad\qquad\quad , \ G_5^{\mathbf{k}} = I_2^g \times J_1^g \\
G_2^{\mathbf{k}} = I_0^g \times J_0^g \ , \ G_3^{\mathbf{k}} = I_1^g \times J_0^g \ , \ G_4^{\mathbf{k}} = I_2^g \times J_0^g
\end{cases} , \tag{65}
$$

  where the stencil ranges are

$$
I_0^g = \{x_{-r}, \ldots, x_{-1}\}, I_1^g = \{x_0, \ldots, x_N\}, I_2^g = \{x_{N+1}, \ldots, x_{N+r}\},
$$
$$
J_0^g = \{y_{-r}, \ldots, y_{-1}\}, J_1^g = \{y_0, \ldots, y_N\}, J_2^g = \{y_{N+1}, \ldots, y_{N+r}\},
$$

  with $N = N_W$.
- **Buffer Area:**
  The Buffer Area is used for the treatment of moving discontinuities. If a high

42

gradient or shock is detected inside a buffer zone, the closest neighboring spectral subdomain(s) is switched to WENO subdomain(s).

For two-dimensional problems, each WENO subdomain has eight "Buffer Zones" $\{B_i^{\mathbf{k}}, \quad i = \mathbf{A}, \ldots, \mathbf{H}\}$ (see the right figure of Figure 12),

$$
\begin{cases}
B_{\mathbf{H}}^{\mathbf{k}} = I_0^b \times J_2^b \ , \ B_{\mathbf{G}}^{\mathbf{k}} = I_1^b \times J_2^b \ , \ B_{\mathbf{F}}^{\mathbf{k}} = I_2^b \times J_2^b \\
B_{\mathbf{A}}^{\mathbf{k}} = I_0^b \times J_1^b \ , \hspace{3.5cm} , \ B_{\mathbf{E}}^{\mathbf{k}} = I_2^b \times J_1^b \\
B_{\mathbf{B}}^{\mathbf{k}} = I_0^b \times J_0^b \ , \ B_{\mathbf{C}}^{\mathbf{k}} = I_1^b \times J_0^b \ , \ B_{\mathbf{D}}^{\mathbf{k}} = I_2^b \times J_0^b
\end{cases} , \tag{66}
$$

where the stencil ranges are given by

$$
I_0^b = \{x_0, \ldots, x_M\}, I_1^b = \{x_{M+1}, \ldots, x_{N-M}\}, I_2^b = \{x_{N-M+1}, \ldots, x_N\},
$$
$$
J_0^b = \{y_0, \ldots, y_M\}, J_1^b = \{y_{M+1}, \ldots, y_{N-M}\}, J_2^b = \{y_{N-M+1}, \ldots, y_N\},
$$

with $N = N_W$ and $M = N_B$. As greater is the value of N_B, earlier is the detection of shocks and gradients, however, at the cost of early switching of the neighboring subdomains to WENO and greater chance of unnecessary costly computations. Satisfactory results have been obtained with the default $M = r$ in this study. It should be noted that these buffer zone grid points are part of the interior grid points and should not be confused with WENO ghost points.

- **Interior Area:**
  Finally, the "Interior Area" is all the WENO grid points $W^{\mathbf{k}}$ excluding the "Ghost Area" and "Buffer Area", $I^{\mathbf{k}} = W^{\mathbf{k}}/(\bigcup_i G_i^{\mathbf{k}} \bigoplus \bigcup_i B_i^{\mathbf{k}})$. If the high gradient stays inside this area, no action is required by the neighbors.

8.2   Interface Conditions

The following configurations are representative of any two-dimensional domain partitions:

- Spectral-Spectral-Spectral-Spectral (Figure 13)
- Spectral-Spectral-Spectral-WENO (Figure 15)
- Spectral-Spectral-WENO-WENO (Figure 15)
- Spectral-WENO-WENO-WENO (Figure 15)
- WENO-WENO-WENO-WENO (Figure 14)

The functional values in the spectral and WENO subdomains are denoted by $s_{ij}^{\mathbf{k}}$ and $w_{ij}^{\mathbf{k}}$ respectively at (x_i, y_j) in the respective subdomain $\mathbf{k}$. Centered at the subdomain $\mathbf{k}$, we define the superscripts $\mathbf{k}_0, \mathbf{k}_1, \mathbf{k}_2, \mathbf{k}_3, \mathbf{k}_4, \mathbf{k}_5, \mathbf{k}_6, \mathbf{k}_7, \mathbf{k}_8$ as

$$
\begin{pmatrix}
\mathbf{k}_8 = \mathbf{k} + (-1,+1) \;,\; \mathbf{k}_7 = \mathbf{k} + (+0,+1) \;,\; \mathbf{k}_6 = \mathbf{k} + (+1,+1) \\
\mathbf{k}_1 = \mathbf{k} + (-1,+0) \;,\; \mathbf{k}_0 = \mathbf{k} \qquad\qquad ,\; \mathbf{k}_5 = \mathbf{k} + (+1,+0) \\
\mathbf{k}_2 = \mathbf{k} + (-1,-1) \;,\; \mathbf{k}_3 = \mathbf{k} + (+0,-1) \;,\; \mathbf{k}_4 = \mathbf{k} + (+1,-1)
\end{pmatrix},
\tag{67}
$$

and they denote the Center ($\mathbf{k}_0$), Left ($\mathbf{k}_1$), Bottom-Left ($\mathbf{k}_2$), Bottom ($\mathbf{k}_3$), Bottom-Right ($\mathbf{k}_4$), Right ($\mathbf{k}_5$), Top-Right ($\mathbf{k}_6$), Top ($\mathbf{k}_7$), and Top-Left($\mathbf{k}_8$) subdomains of subdomain $\mathbf{k} = \mathbf{k}_0$ respectively. For example $s_{ij}^{\mathbf{k}_1}$ is to be interpreted as a value at the point (x_i, y_j) in the spectral Left subdomain $\mathbf{k}_1 = \mathbf{k} + (-1,+0)$. The subdomain interfaces consist of corners and shared sides among the spectral and WENO subdomains.

Spectral-Spectral Interface
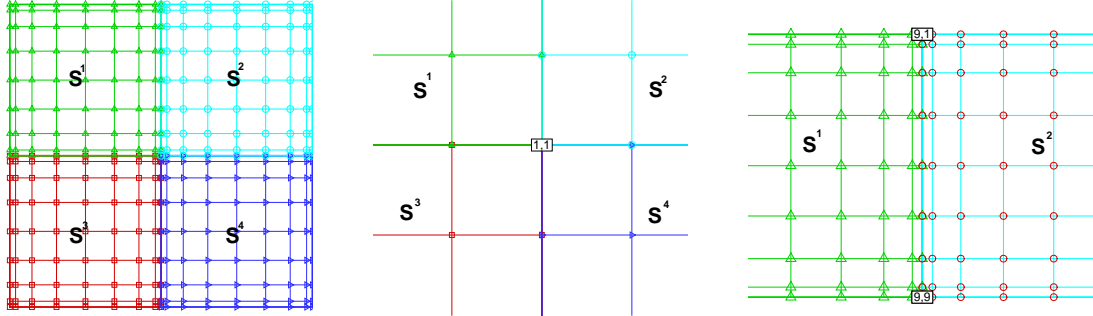
Fig. 13. (Left) Spectral-Spectral-Spectral-Spectral subdomains configuration. (Middle) Corner point of all four spectral subdomains. (Right) Shared side of two spectral subdomains.

Corners only appear at the connection of two or more spectral subdomains, since the grid points of the WENO subdomains never coincide with the spectral collocation points at the interface. Corner values are assigned with the average of the values of all connecting subdomains. For example, in figure 13, assuming that S^1 is the reference subdomain $\mathbf{k}_0$ and $N = N_s$,

$$
s_{0N}^{\mathbf{k}_0} = s_{00}^{\mathbf{k}_3} = s_{N0}^{\mathbf{k}_4} = s_{NN}^{\mathbf{k}_5} = \frac{1}{4}\left(s_{0N}^{\mathbf{k}_0} + s_{00}^{\mathbf{k}_3} + s_{N0}^{\mathbf{k}_4} + s_{NN}^{\mathbf{k}_5} \right).
\tag{68}
$$

44

Along the interface between two spectral subdomains, the values at the shared side are computed similarly by assigning the average of the two values of the connected subdomains at all collocation points. Consider the interface between the two spectral subdomains $S^1 - S^2$ (the rightmost figure of Figure 13),

$$s_{0j}^{\mathbf{k}_0} = s_{Nj}^{\mathbf{k}_5} = \frac{1}{2}\left(s_{0j}^{\mathbf{k}_0} + s_{Nj}^{\mathbf{k}_5}\right), \quad j = 0, \ldots, N. \tag{69}$$

The other spectral subdomains' corners and sides are treated similarly.

Note 8.1. *In case of adjacent subdomains with different numbers of collocation points, global interpolation can be used before averaging.*

Note 8.2. *An exact Riemannn solver and penalty interface conditions had been tried but no discernible differences were observed from the simple average.*

WENO-WENO Interface

To maintain conservation, adjacent WENO subdomains are required to have the same spacing Δx (see [28]). This implies that ghost points of a WENO subdomain match the interior points of the neighboring WENO subdomain (see Figure 14). Thus, simple copying of the solution values of the neighboring interior points to the "Ghost Area" is sufficient for the communication of WENO subdomains.
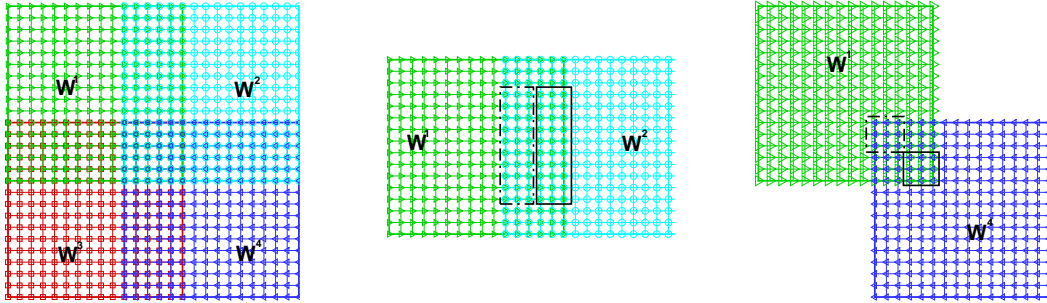
Fig. 14. (Left) WENO-WENO-WENO-WENO subdomain configuration. (Middle) $W^1 - W^2$ Interface. (Right) $W^1 - W^4$ Interface.

For instance the middle figure of Figure 14 shows two "Ghost Zones": The zone in the solid rectangle corresponds to the "Ghost Zone" $G_5^{\mathbf{k}}$ of W^1; and the zone in the dash-dotted rectangle corresponds to the "Ghost Zone" $G_1^{\mathbf{k}}$ of W^2 (see 65). In this case, by denoting $N = N_W$ and using W^1 as a reference subdomain (subdomain $\mathbf{k} = \mathbf{k}_0$)

$$w_{(N+l)j}^{\mathbf{k}_0} = w_{lj}^{\mathbf{k}_5}, \quad w_{-lj}^{\mathbf{k}_5} = w_{(N+1-l)j}^{\mathbf{k}_0}, \quad j = -r, \ldots, N+r, \quad l = 1, \ldots, r, \tag{70}$$

45

where r is the number of ghost points.

Note 8.3. *In general the number of "ghost" points in each subdomain does not have to be the same as long as the same grid spacing Δx is used at all the neighboring subdomains.*

Spectral-WENO Interface

Spectral-WENO interface can be found in the configurations shown in Figure 15.
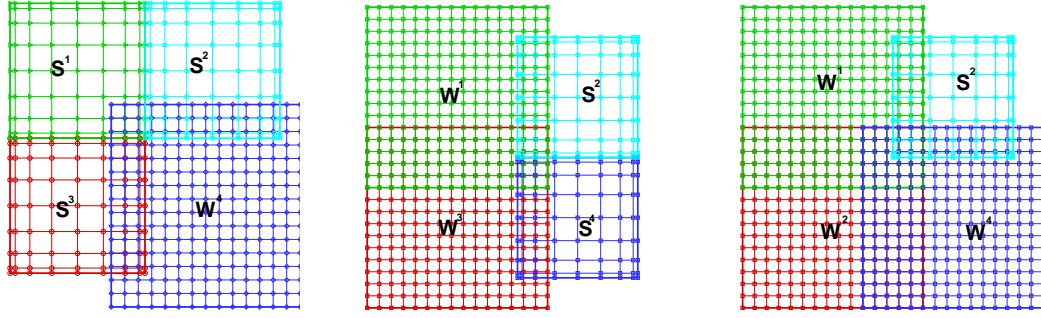

Fig. 15. Subdomain Configurations: (Left) Spectral-Spectral-Spectral-WENO. (Middle) Spectral-Spectral-WENO-WENO. (Right) Spectral-WENO-WENO-WENO.
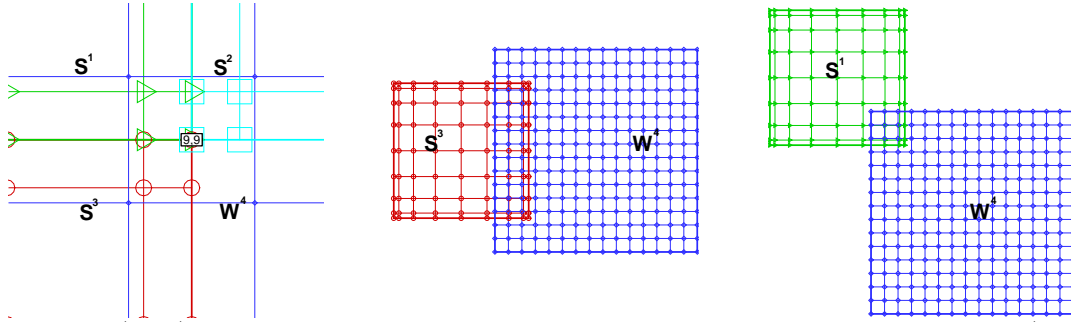

Fig. 16. (Left) Spectral-Spectral-Spectral-WENO subdomain configuration. (Middle) $S^3 - W^4$ Interface. (Right) $S^1 - W^4$ Interface.

The "Ghost Zones" $G_2^{\mathbf{k}}, G_7^{\mathbf{k}}$ and $G_8^{\mathbf{k}}$ of the WENO subdomain lie in the three neighboring spectral subdomains as shown in Figure 15. The "Ghost Area" points of WENO subdomains are computed via spectral interpolations. To be more specific, referring to the middle figure of Figure 16, the solution in the area of the intersection of S^3 (subdomain $\mathbf{k}$) and W^4 (subdomain $\mathbf{k}_5$) corresponding to the "Ghost Zone" $G_1^{\mathbf{k}}$ in (65) (see also Figure 12) is read using the interpolating polynomial representing the

solution in S^3, that is, at the subdomain $\mathbf{k}$,

$$w(x_n, y_m) = \sum_{j=0}^{N_S} \sum_{i=0}^{N_S} s_{ij} l_i(x_n) l_j(y_m), \quad m = 0, \ldots, N_W, \quad n = -r, \ldots, -1, \quad (x_n, y_m) \in \mathbf{k}_5,$$

$$(71)$$

where s_{ij} are the functional values in S^3 (subdomain $\mathbf{k}$), $l_i(x)$ and $l_j(y)$ are Lagrangian interpolation polynomials of degree N_s. The ghost points for the other two configurations can be obtained in a similar way.

The interface points of the spectral subdomain are computed via a two dimensional interpolation polynomial of degree $r = n_W$. The choice of stencils $\{(x_i, y_j), i = -i_0 - r/2, \ldots, i_0 + r/2, j = j_0 - r/2, \ldots, j_0 + r/2\}$ for the interpolation polynomial should be as symmetric about a given point (x_{i_0}, y_{j_0}) as possible.

8.3 The Switching Algorithm

In this section we describe the algorithm used to switch the subdomains spatial discretizations as indicated by the Multi-Resolution Analysis of Section 7. The following three conditions are the main rules to be followed:

(1) If a subdomain contains high gradients, then switch its spatial discretization to (or keep it with) WENO;
(2) If high gradients are present in the "Buffer Areas" of connected neighboring subdomains, then switch the current subdomain to (or keep it as) a WENO subdomain;
(3) In any other case, switch the subdomain to (or keep it as) a spectral subdomain;

The first condition above avoids the Gibbs phenomenon, keeping the discontinuities inside WENO subdomains. The second condition ensures the switch to WENO subdomain in order to allow only WENO-to-WENO transmission of discontinuities. The third condition improves the numerical efficiency, since it ensures that smooth parts of the solution will always be contained in spectral subdomains.

Multi-Resolution analysis of the solution is performed at every sub-stage of the third order TVD Runge-Kutta scheme used for the temporal evolution. At each subdomain $\mathbf{k}$, we define the smoothness flag variable, $\text{Flag}_{ij}^{\mathbf{k}}$, at each grid point (x_i, y_j) including

the ghost points, as ,

$$\text{Flag}_{ij}^{\mathbf{k}} = \begin{cases} 1, \ |d_{ij}^{\mathbf{k}}| > \epsilon_{MR} & \text{for} \quad (x_i, y_j) \subseteq I^{\mathbf{k}} \oplus B_l^{\mathbf{k}} \quad l = \mathbf{A}, \dots, \mathbf{H} \\ 0, \ \text{otherwise} \end{cases} . \qquad (72)$$

where $d_{ij}^{\mathbf{k}}$ are the MR coefficients. Since the Multi-Resolution Analysis requires uniformly spaced grids, the spectral grids are first interpolated to uniformly spaced grids before obtaining the MR coefficients $d_{ij}^{\mathbf{k}}$. The necessary ghost points are acquired from the neighboring subdomains. At the boundary subdomains, the value of the boundary ghost points are extrapolated linearly from the interior data.

The algorithm proceeds by checking for each subdomain $\mathbf{k}$ and at the buffer zones of the neighboring subdomains if $\text{Flag}_{ij}^{\mathbf{k}}$ is equal to one. If so, it switches subdomain $\mathbf{k}$ to a WENO discretization. On the other hand, if $\text{Flag}_{ij}^{\mathbf{k}}$ is identically zero, then a spectral discretization is implemented, or kept. These switches require the use of interpolation from a Chebyshev grid of points to a uniformly spaced one and vice-versa:

- To switch from the spectral subdomain to the WENO subdomain, the data are interpolated onto the uniformly spaced grid via the spectral interpolation formula.
- To switch from the WENO subdomain to the spectral subdomain, the data are interpolated onto the Chebyshev Gauss-Lobatto points via the Lagrangian interpolation polynomial of the same order as the WENO method.

Back and forth switching between WENO and spectral discretizations may occur too frequently for the same domain when the ϵ_{MR} is marginally set. The $d_{ij}^{\mathbf{k}}$ coefficients might oscillate around the parameter ϵ_{MR} in time due to some numerical factors such as dissipation, dispersion and nonlinear effects, or any combination of such. This pattern of switching can repeat itself for a while until the solution settles down with a clear definition of the $d_{ij}^{\mathbf{k}}$, which is either greater than or smaller than the MR tolerance ϵ_{MR}. In order to alleviate such occurrences, one must devise a procedure preventing the switch from WENO to spectral if it had already occurred recently. However, the procedure must never prevent a spectral to WENO switch, for oscillations and instability might occur.

9 Numerical Results

In this section, we apply the hybrid method to two well-known problems in Conservation Laws: The Shock-Vortex Interaction and the Richtmyer-Meshkov Instability. The governing equations are the two-dimensional Euler equations in Cartesian coordinates given by:

$$\mathbf{Q}_t + \mathbf{F}_x + \mathbf{G}_y = 0, \tag{73}$$

where

$$
\begin{aligned}
\mathbf{Q} &= (\rho, \rho u, \rho v, E)^T, \\
\mathbf{F} &= \left(\rho u, \rho u^2 + P, \rho u v, (E + P)u\right)^T, \\
\mathbf{G} &= \left(\rho v, \rho u v, \rho v^2 + P, (E + P)v\right)^T,
\end{aligned}
\tag{74}
$$

and the Equation of state

$$P = (\gamma - 1)(E + \tfrac{1}{2}\rho\left(u^2 + v^2\right)), \qquad \gamma = 1.4. \tag{75}$$

We will restrict the following study to rectangular domains, which will be partitioned into an equal number of subdomains in both x and y directions. The number of Chebyshev collocation points for all spectral subdomains will be the same in both x and y directions, as well as the number of uniformly spaced grid points for the WENO subdomains. The order of the Multi-Resolution Analysis is the same as the WENO scheme, $n_{MR} = n_W$. A 14_th order Exponential filter and Kosloff-Tal-Ezer mapping are employed in all spectral subdomains. Free stream boundary conditions are imposed in the inflow and outflow in the x direction and periodical boundary condition is imposed in the y direction. To evolve the ODE from the semi-discretized PDE in time, the third order Total Variation Diminishing Runge-Kutta scheme (RK-TVD) will be used [4]:

$$
\begin{aligned}
\vec{U}^1 &= \vec{U}^n + \Delta t L(\vec{U})^n \\
\vec{U}^2 &= \frac{1}{4}\left(3\vec{U}^n + \vec{U}^1 + \Delta t L(\vec{U}^1)\right), \\
\vec{U}^{n+1} &= \frac{1}{3}\left(\vec{U}^n + 2\vec{U}^2 + 2\Delta t L(\vec{U}^2)\right)
\end{aligned}
\tag{76}
$$

where L is the spatial operator. The CFL numbers for the spectral and WENO subdomains are set to be 3 and 0.4, respectively. All numerical experiments were run

on a 667 MHz Compaq Alpha machine with 1GB memory and with an Alpha internal floating point processor.

9.1   Shock – Vortex Interaction

The tangential velocity profile of the counter-clockwise rotating vortex [21] centered at (x_c, y_c) and strength Γ is given in polar coordinates by:

$$U(r) = \begin{cases} \Gamma r(r_0^{-2} - r_1^{-2}) & 0 \le r \le r_0 < r_1 \\ \Gamma r(r^{-2} - r_1^{-2}) & r_0 \le r \le r_1 \\ 0 & r > r_1 \end{cases} , \tag{77}$$

where $r_0 = 0.2$ and $r_1 = 1.0$.

Due to the strong nonlinearity of the shock-vortex interaction its physics are not well understood. A better understanding will have many potential applications, for instance, subsonic and supersonic jet nozzle design and blade noise generation. The Hybrid method will be tested on this problem with a vortex of amplitude $\Gamma = 0.25$ and shock Mach numbers $M_s = 1.25, 3, 6$.

Mach 1.25

In this first example, the physical domain $(0 \le x \le 3.9, -2 \le y \le 2)$ is partitioned into a 13×10 grid of subdomains. Spectral subdomains use a 32×32 grid of Chebyshev points and WENO grids are 50×50. MR analysis is performed with the MR tolerance set to $\epsilon_{MR} = 5 \times 10^{-2}$.

When an initially planar shock wave hits the vortex, it deforms as compression and rarefaction regions are created behind the shock, as shown in Figure 17 for $t = 0.732, 1.08, 1.2$. As the interaction proceeds over time, strong bifurcation and deformation of the shock are observed. The shock emanating from the compression region has one part moving upward and another moving downward. The strength of the lower upward moving part is greater, due to the direction of rotation of the vortex. MR Analysis performed well in capturing the shock and the high gradient regions
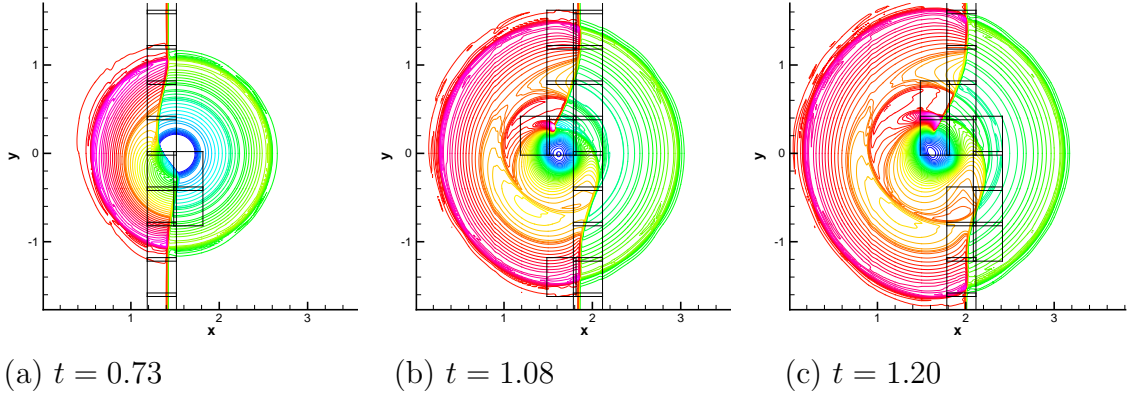
50

(a) $t = 0.73$ (b) $t = 1.08$ (c) $t = 1.20$

Fig. 17. Density ρ of the Shock-Vortex interaction with Mach number $M_s = 1.25$ and $\Gamma = 0.25$ at (a) $t = 0.73$, (b) $t = 1.08$ and (c) $t = 1.2$, as computed by the Hybrid method.

immediately behind the shock, as indicated by the WENO subdomains enclosed with black bounding boxes. The remaining subdomains are accurately dealt with by the spectral methods. The number of WENO subdomains is far fewer than spectral ones resulting in a more efficient algorithm than the classical WENO scheme.

Mach 3

We now increase the Mach number of the shock from $M_s = 1.25$ to $M_s = 3$ and compare the solution of the Hybrid scheme with a highly resolved one computed with the classical fifth order WENO scheme using 1200×1200 points. The physical domain $(0 \le x \le 3.0, -2 \le y \le 2)$ is partitioned into a 10×10 grid of subdomains and all other parameters are as in Example 1.

As in the previous example, an acoustic wavefront is generated and a number of fine scale structures are formed behind the main shock. This example indicates that the Hybrid method captures the fine features of the solution even in the case of strong shocks.
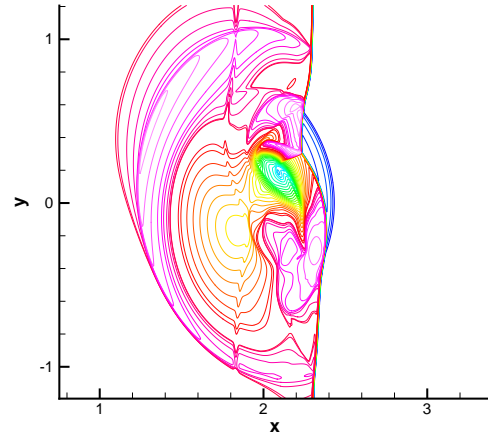
51
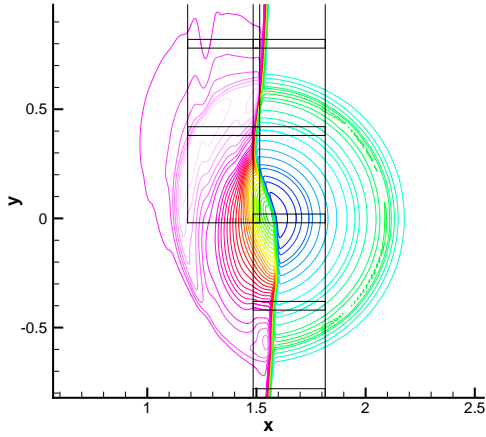
(a) $t = 0.35$, Hybrid Scheme
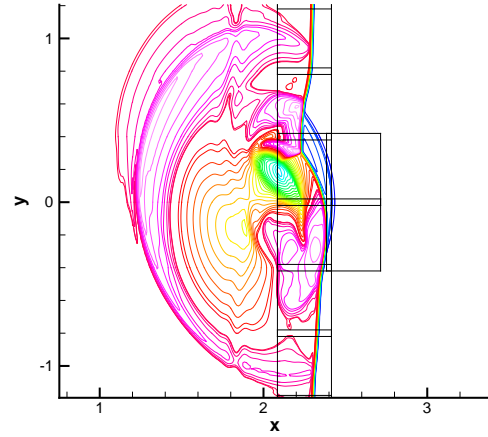
(b) $t = 0.60$, Hybrid Scheme
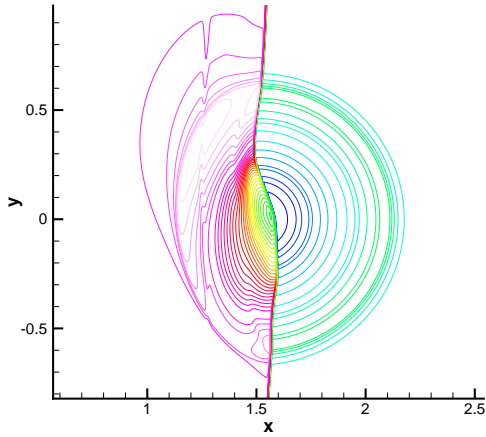
(c) $t = 0.35$, WENO5 Scheme

(d) $t = 0.60$, WENO5 Scheme

Fig. 18. Density ρ of the Shock-Vortex interaction with Mach number $M_s = 3$ and $\Gamma = 0.25$ at time (a) $t = 0.35$ and (b) $t = 0.6$ as computed by the Hybrid scheme and (c) $t = 0.35$ and (d) $t = 0.6$ as computed by the classical fifth order WENO finite difference scheme (WENO5) with 1200×1200 grid points.

Mach 6

In this last example, we further increase the shock Mach number to $M_s = 6$ and use a 19×20 grid of subdomains to partition the physical domain ($0 \leq x \leq 4.2, -3 \leq y \leq 3$). The spectral grid is 16×16. This example shows that the Hybrid method can be applied to higher Mach number flows as well, still resulting on a reliable and efficient shock-capturing method.

52

(a) $t = 0.3$ (b) $t = 0.4$
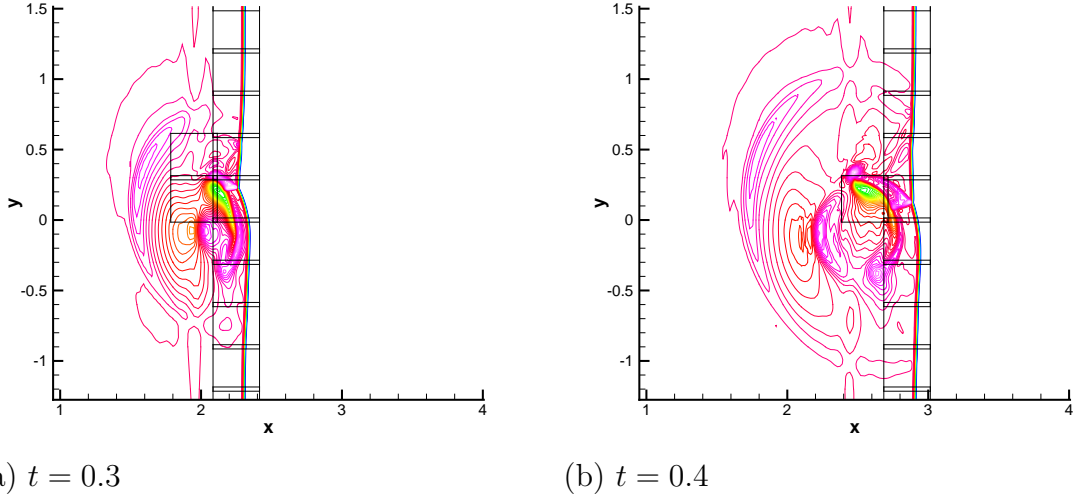
Fig. 19. Density ρ of the Shock-Vortex interaction with Mach number $M_s = 6$ and $\Gamma = 0.25$ at time (a) $t = 0.3$ and (b) $t = 0.4$ as computed by the Hybrid method.

9.2 Two-dimensional Richtmyer-Meshkov Instability

Richtmyer in 1960 [26] theoretically predicted the occurrence of instability on a perturbed material interface under the impulsive acceleration of an incident shock wave. In 1970 Meshkov [24] experimentally confirmed these predictions. A variety of motions can be generated following the interaction of a shock wave with an interface separating two materials. Any small perturbation present on the interface will be amplified after such a contact. This class of problems is referred in the literature as the "Richtmyer-Meshkov Instability (RMI)". As the interface between two materials becomes increasingly distorted other instabilities such as the Kelvin-Helmholtz Instabilities develop and a region of turbulence mixing ultimately results. The RMI arises in many applications as, for instance, the Inertial Confinement Fusion (ICF) process. A recent model under extensive study consists of a set of laser beams directed into a chamber containing a spherical fusion fuel target. The expected result should be compression, ignition and a subsequent energy surplus. However, since no perfect capsule exists, irregularities on the surface excite the undesirable RMI, reducing the effective uniform compression pressure onto the capsule.

Fig. 20. Initial Condition for the Richtmyer-Meshkov Instability simulation
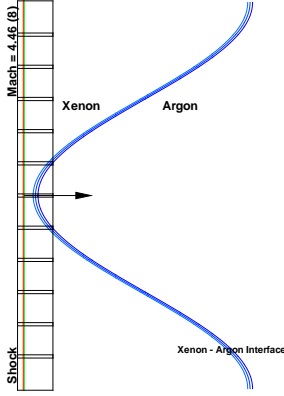
1) Rankine-Hugoniot condition for shocks
2) Pre-Shock Temperature $T = 296$ K
3) Pre-Shock Pressure $P = 0.5$ atm
4) Xenon density $\rho_{Xe} = 2.90 \times 10^{-3} \frac{\text{g}}{\text{cm}^3}$
5) Argon density $\rho_{Ar} = 0.89 \times 10^{-3} \frac{\text{g}}{\text{cm}^3}$
6) Specific heat ratio $\gamma = \frac{5}{3}$
7) Atwood number $At = 0.54$
8) Mach number $M = 4.46$
9) Wave Length $\lambda = 3.6$cm
10) Amplitude $a = 1.0$cm
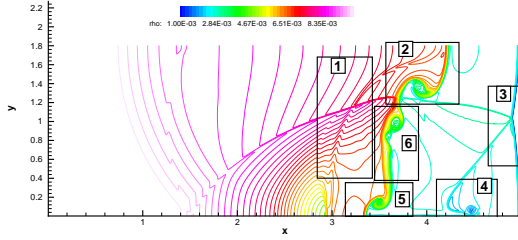
Regions of Interest :

1) Reflected shock generated by the shock refraction;
2) The penetration of the heavy (Xe) to light (Ar) gas forms the Spike;
3) Triple point on the transmitted shock;
4) A small jet and its vortical structure;
5) The penetration of the light (Ar) to heavy (Xe) gas forms the Bubble;
6) Vortical rollups of the gaseous interface.

Fig. 21. Typical regions of interest for the simulation of the RMI at time $t = 50\,\mu s$. Only the lower half of the interface is shown.

Presently, a rectangular domain with a shock Mach number M_s interacting with a single mode sinusoidal perturbation along a Xenon (Xe) and Argon (Ar) gases interface is simulated using the Hybrid method. The initial condition is given in Figure 20 and a diffusive interface is modeled with an exponential function, i.e.

$$S(x,y) = \begin{cases} 1 & d \leq 0 \\ \exp(-\alpha|d|^{\beta}) & 0 < d < 1, \\ 0 & d \geq 1 \end{cases} \tag{78}$$

where

$$d = \frac{(x_s + a\cos(2\pi y/\lambda) + \delta) - x}{2\delta}, \tag{79}$$

54

$\delta = 0.2$cm > 0 is the interface thickness, $\beta = 8$ is the interface order, $x_s = 0.5$cm is the location of the interface and $\alpha = -\ln \epsilon$, where ϵ is the machine zero. The conservative or primitive variables are scaled according to the $S(x, y)$ between the Xenon and Argon gases.

As the shock wave collides with the interface separating the two gases, the sine wave perturbation is accelerated, compressed and amplified following the refraction of the shock. The heavier Xenon gas (Xe) will penetrate into the lighter Argon gas (Ar) forming finger-like structures – bubbles and spikes. A bubble (spike) is a portion of the light (heavy) gas penetrating into the heavy (light) gas. Some of these interesting fluid structures such as the bubbles, the spikes, the interfacial mixing region and the vortical rollup can be observed at the earlier time as depicted in Figure 21.

The basic mechanism of these instabilities is the baroclinic generation of vorticity $\vec{\omega}$ induced from the misalignment of the pressure gradient ∇p of the shock and the local density gradient $\nabla \rho$ across the interface:

$$\frac{\partial \vec{\omega}}{\partial t} \sim \nabla p \times \nabla \rho, \qquad \vec{\omega} = \nabla \times \vec{u}, \tag{80}$$

where $\vec{u}$ is the velocity.

Mach 4.46

In this example, the physical domain $(0 \leq x \leq 5.1, 0 \leq y \leq \lambda)$ is partitioned into a 17×12 grid of subdomains. The spectral grids are 32×32 and the WENO grids are 50×50. The MR tolerance is now lowered to $\epsilon_{MR} = 5 \times 10^{-5}$. Once again, as seen in Figure 22, the WENO method is activated only along the material interface and where high gradients appear.
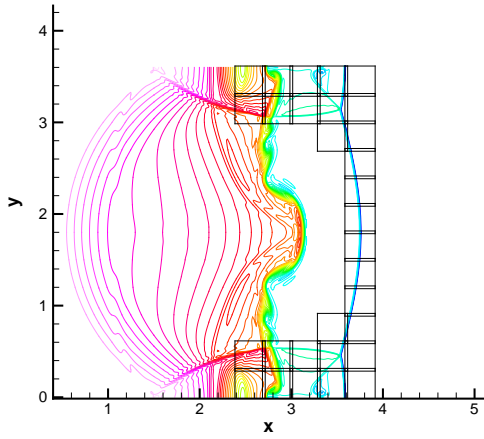
Mach 8

The physical domain $(0 \leq x \leq 24.6, 0 \leq y \leq \lambda)$ is partitioned into a 82×12 grid of subdomains in order to apply the Hybrid method for a longer time integration up to $t = 100 \mu s$. The shock Mach number is increased from $M_s = 4.46$ to $M_s = 8$ and the spectral grid is set to 24×24.
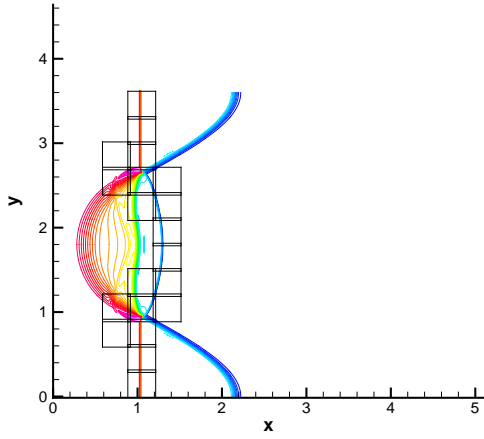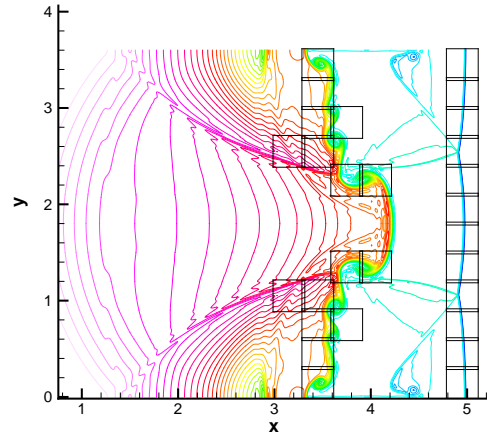
(a) $t = 12.5\,\mu s$
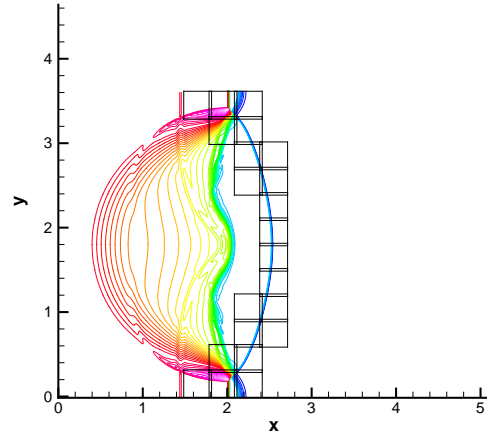
(b) $t = 25.0\,\mu s$

(c) $t = 37.5\,\mu s$

(d) $t = 50.0\,\mu s$

Fig. 22. Contour plot of the density ρ with $M_s = 4.46, \lambda = 3.6$cm, $a = 1$cm at time (a) $t = 12.5\,\mu s$, (b) $t = 25.0\,\mu s$, (c) $t = 37.5\,\mu s$ and (d) $t = 50.0\,\mu s$ of the Richtmyer-Meshkov Instability as computed by the Hybrid scheme.
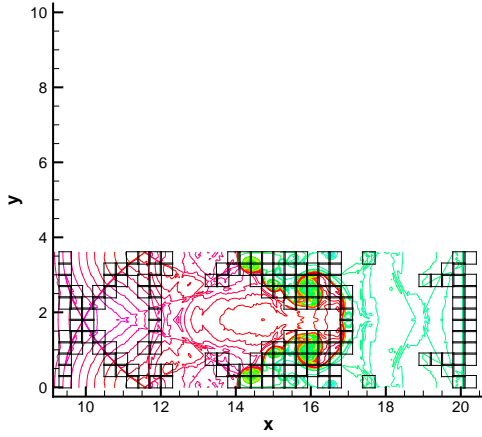
It can be observed in Figure 23 that the Hybrid method successfully tracks shocks and high gradients with WENO discretization (black bounding boxes) while the smooth parts of the solution are well represented using spectral subdomains.
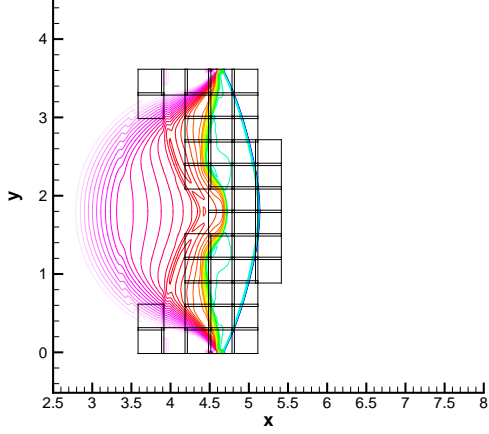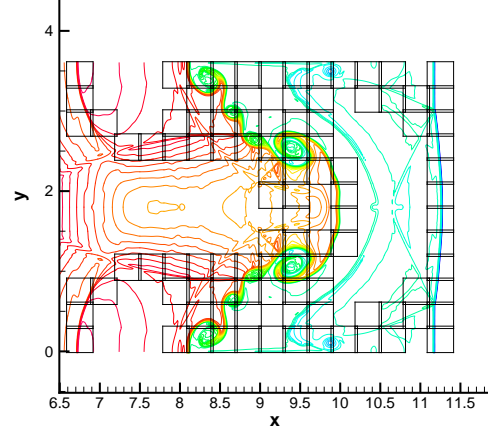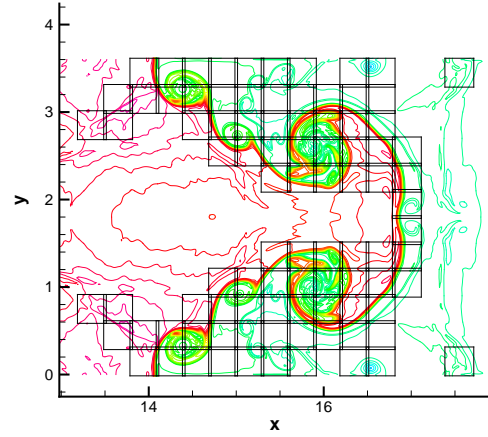
(a) $t = 18.5\,\mu s$ (b) $t = 52.0\,\mu s$

(a) $t = 100.0\,\mu s$ (b) $t = 100.0\,\mu s$ with zoom

Fig. 23. Contour plot of the density ρ with $M_s = 8, \lambda = 3.6$cm, $a = 1$cm at time (a) $t = 18.5\,\mu s$, (b) $t = 52.0\,\mu s$, (c) $t = 100.0\,\mu s$ and (d) $t = 100.0\,\mu s$ with zoom of the Richtmyer-Meshkov Instability as computed by the Hybrid scheme.

9.3 CPU Timing

The Hybrid method has the potential advantage of being faster than the classical WENO method due to the higher numerical efficiency of spectral methods at smooth parts of the solution. Moreover, spectral discretizations avoid the expensive characteristic decompositions and projections of the WENO method. In this section, we provide some CPU timing results for the Mach 3 Shock-Vortex Interaction (see section 9.1) when using the Hybrid and the classical WENO methods with equal resolution.

The physical domain is partitioned into a set of subdomains of sizes $((10 \times 2^j) \times (10 \times 2^j)), j = 0, 1, 2, 3$. Spectral subdomains use a 12×12 grid of Chebyshev points and WENO ones use 20×20 grids of uniformly spaced points. The classical fifth-order WENO method, here denoted WENO5, uses the corresponding number of grid points as if all the subdomains in the Hybrid method were WENO subdomains. The MR tolerance used is $\epsilon_{MR} = 5 \times 10^{-2}$.

Number of subdomains	Grid size	Hybrid S12W20	WENO5	Speedup
10x10	200x200	265	282	1.06
20x20	400x400	2009	2762	1.37
40x40	800x800	14410	26090	1.81
80x80	1600x1600	112900	253996	2.24

Table IX
CPU timing in seconds and speedup factor for the Shock-Vortex problem at time $t = 0.6$ as computed by the Hybrid (with constant $\epsilon_{MR} = 5 \times 10^{-2}$) and the WENO5 methods.

Table IX shows that a significant speed up is achieved when using the Hybrid method over the classical WENO5 for increasing resolution. Figure 24 shows the history of the coverage of the WENO subdomains as a percentage of the total number of the subdomains. This percentage varies between $10\% - 20\%$ for the 10×10 subdomain partition and gets proportionally smaller by a factor of 2 when the number of subdomain partition increases by a factor of 2 in each direction.
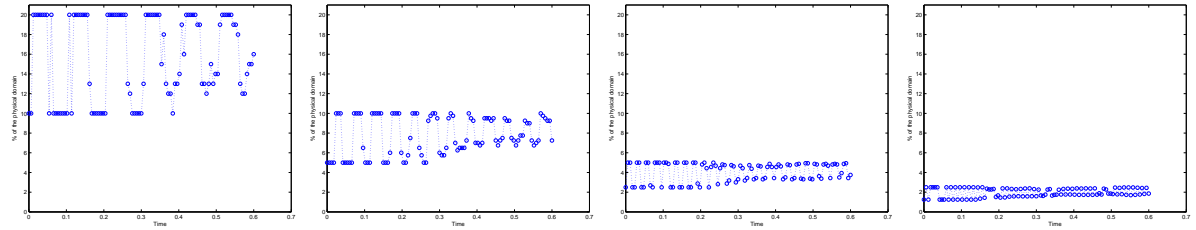

Fig. 24. The time history of the coverage of the WENO subdomains as a percentage of total number of subdomains for the four subdomain partitions: (from left to right) $(10 \times 10), (20 \times 20), (40 \times 40), (80 \times 80)$.

Reducing the MR Tolerance level of last experiment to $\epsilon_{MR} = 5 \times 10^{-3}$, while keeping all the other parameters fixed, leads to a slight increase on the CPU time usage for the Hybrid method as compared with the previous case, as shown in Table X. With a lower MR tolerance, more subdomains are classified as containing high gradients.

Number of subdomains	Grid size	Hybrid S12W20	WENO	Speedup
10x10	200x200	332	282	none
20x20	400x400	2239	2762	1.23
40x40	800x800	15580	26090	1.67

Table X

CPU timing in seconds and speedup factor for the Shock-Vortex problem at time $t = 0.6$ as computed by the Hybrid (constant $\epsilon_{MR} = 5 \times 10^{-3}$) and WENO5 methods.

References

[1] J. P. Boris and D. L. Book. Flux Corrected Transport I, SHASTA, a Fluid Algorithm that Works. *J. Comput. Phys*, 11:38–69, 1973.

[2] C. Canuto, A. Quarteroni, M.Y. Hussaini, and T. Zang. *Spectral Methods in Fluid Mechanics*. Springer-Verlag, New York, 1988.

[3] Q.-Y. Chen, D. Gottlieb, and J.S. Hesthaven. Uncertainty analysis for the steady-state flows in a dual throat nozzle. *J. Comput. Phys.*, 204:387–398, 2005.

[4] B. Cockburn, C. Johnson, C.-W. Shu, and E. Tadmor. *Advanced Numerical Approximation of Nonlinear Hyperbolic Equations*, volume 1697 of *Lecture Notes in Mathematics*, chapter Essentially Non-Oscillatory and Weighted Essentially Non-Oscillatory Schemes for Hyperbolic Conservation Laws, pages 325–432. Springer, Cetraro, Italy, 1997. Editor: A. Quarteroni.

[5] B. Costa and W.-S. Don. On the Computation of High Order PseudoSpectral Derivatives. *Applied Numerical Mathematics*, 33:151–159, 2000.

[6] W.-S. Don. Numerical Study of PseudoSpectral Methods in Shock Wave Applications. *J. Comput. Phys.*, 110(1):103–111, 1994.

[7] W.-S. Don and B. Costa. Multi-Domain Hybrid Spectral-WENO Methods for Conservation Laws. In preparation.

[8] W.-S. Don and A. Solomonoff. Accuracy and Speed in Computing the Chebyshev Collocation Derivative. *SIAM, J. Sci. Comput.*, 16(6):1253–1268, November 1995.

[9] W.-S. Don and A. Solomonoff. Accuracy Enhancement for Higher Derivatives using Chebyshev Collocation and a Mapping Technique. *SIAM, J. Sci. Comput.*, 18(4):1044–1055, July 1997.

[10] R.G. Ghanem. Ingredients for a general purpose stochastic finite element formulation. *Comput. Methods Appl. Mech. Engrg.*, 168:19–34, 1999.

[11] R.G. Ghanem and P. Spanos. *Stochastic Finite Elements: a Spectral Approach*. Springer-Verlag, 1991.

[12] D. Gottlieb, L. Lustman, and C. S. Streett. *Spectral Methods for Partial Differential Equations*, chapter Spectral Methods for Two Dimensional Shocks, page 79. SIAM-CBMS. Society for Industrial and Applied Mathematics, Philadelphia, 1984. Edited by R.G. Voigt and D.Gottlieb and M.Y. Hussaini.

[13] D. Gottlieb and S. Orszag. *Numerical Analysis of Spectral Methods: Theory and Applications.* Society for Industrial and Applied Mathematics, Philadelphia, 1977.

[14] D. Gottlieb and S.A. Orszag. *Numerical Analysis of Spectral Methods: Theory and Applications.* CBMS-NSF, SIAM, Philadelphia, PA, 1977.

[15] D. Gottlieb, C.-W. Shu, A. Solomonoff, and H. Vandeven. On the Gibbs Phenomenon I: Recovering Exponential Accuracy from the Fourier Partial Sum of a Nonperiodic Analytic Function. *J. Comput. Appl. Math*, 43:81–92, 1992.

[16] A. Harten. High Resolution Schemes for Hyperbolic Conservation Laws. *J. Comput. Phys.*, 49:357–393, 1983.

[17] A. Harten. Adaptive Multiresolution Schemes for Shock Computations. *J. Comput. Phys.*, 115:319–338, 1994.

[18] A. Harten, B. Engquist, S. Osher, and S. Chakravarthy. Uniformly High-Order Accurate Essentially Non-Oscillatory Schemes III. *J. Comput. Phys.*, 71:231–303, 1987.

[19] G. Jiang and C.-W. Shu. Efficient Implementation of Weighted ENO Schemes. *J. Comput. Phys.*, 126:202–228, 1996.

[20] J.-H. Jung and B. D. Shizgal. Generalization of the Inverse Polynomial Reconstruction Method in the Resolution of the Gibbs Phenomenon. *J. Comput. Applied Math.*, 172(1):131–151, 2004.

[21] D. A. Kopriva. A Multidomain Spectral Collocation Computation of the Sound Generated by a Shock-Vortex Interaction. *Computational Acoustics: Algorithms and applications*, 2, 1988. D. Lee and M. H. Schultz (eds.).

[22] D. Kosloff and H. Tal-Ezer. Modified Chebyshev PseudoSpectral Methods with $O(N^{-1})$ Time Step Restriction. *J. Comput. Phys.*, 104:457–469, 1993.

[23] X.-D. Liu, S. Osher, and T. Chan. Weighted Essentially Non-Oscillatory Schemes. *J. Comput. Phys.*, 115:200–212, 1994.

[24] E. E. Meshkov. Instability of a Shock Wave Accelerated Interface between Two Gases. *NASA*, F-13:074, 1970.

[25] M.-S. Min, M. S. Kaber, and W.-S. Don. Fourier-Padé Approximations and Filtering for the Spectral Simulations of Incompressible Boussinesq Convection Problem. *Publications du Laboratorie Jacques-Louis Lions, R03021, Mathematics of Computation*, 2004.

[26] R. D. Richtmyer. Taylor Instability in Shock Acceleration of Compressible Fluids. *Comm. Pure Appl. Math*, 13:297–319, 1960.

[27] P. L. Roe. Approximate Riemann Solvers, Parameter Vectors, and Difference Schemes. *J. Comput. Phys.*, 43:357–372, 1981.

[28] K. Sebastian. *Multi Domain Weighted Essentially Non Oscillatory (WENO) Method With Interpolation at Subdomain Interfaces.* PhD thesis, Brown University, May 2003.

[29] B. van Leer. Towards the Ultimate Conservative Difference Scheme. A Second Order Sequel of Godunov's Method. *J. Comput. Phys.*, 32:101–136, 1979.

[30] H. Vandeven. Family of Spectral Filters for Discontinuous Problems. *J. Sci. Comput.*, 8:159–192, 1991.

[31] N. Wiener. The homogeneous chaos. *Amer. J. Math.*, 60:897–936, 1938.

[32] D. Xiu and G.E. Karniadakis. The Wiener-Askey polynomial chaos for stochastic differential equations. *SIAM J. Sci. Comput.*, 24(2):619–644, 2002.

[33] D. Xiu and G.E. Karniadakis. Modeling uncertainty in flow simulations via generalized polynomial chaos. *J. Comput. Phys.*, 187:137–167, 2003.

10   High Order Simulation of the Richtmyer-Meshkov Instability

We also, in collaboration with Dr. Oleg Schilling at the Lawrence Livermore National Laboratory (LLNL) pursuing the investigation of the high order WENO methods for the three dimensional Richtmyer-Meshkov Instability. We have recently extended the Euler Equation to the full Navier-Stokes equation with multiple species in two and three dimensions. We are also in the process of implementing a full turbulence analysis routines for real time data extraction and analysis.

A systematical and self-consistent study was conducted to validate the WENO methods for the RMI problems with reshock against the Mach 1.21 shock tube experiments of Collins and Jacobs. The qualitative comparison above shows that it is possible to achieve very good agreement between a two-dimensional, high-resolution shock-capturing simulation with high-order flux reconstruction and experimental density PLIF images. The simulations at 5 and 6 ms demonstrates that higher-order reconstruction better captures secondary instabilities on the interface and within the vortex cores. The reshock takes place at about $t = 5.75$ ms. In addition, the roll-ups in the simulation appear tighter and sharper, and more fine-scale structures are present. The fields from the numerical simulations also supplement the experimental images by displaying the shock focusing observed during the reshock process. This results in the formation and persistence of large-scale structures in the simulations, consistent with the inverse cascade of kinetic energy from small scales to larger scales observed in experiments and simulations of two-dimensional turbulence.

As the results of this study, we have published three papers in the Physics of Fluids, Journal of Computational Physics and Physics Review E. More details can be found in those publications.

11 Galerkin Method for Wave Equations with Uncertain Coefficients

In recent years there is a growing interests in studying efficient numerical methods for solving differential equations with random inputs. The Polynomial Chaos (PC) based methods have received intensive attention. The original PC method was developed by R. Ghanem, cf. [11], and was inspired by the Wiener chaos expansion which uses Hermite polynomials of Gaussian random variables to represent random processes [31]. Later the approach was extended to generalized Polynomial Chaos (gPC) where general orthogonal polynomials are adopted for improved representations of more general random processes [32]. With PC/gPC serving as a complete basis to represent random processes, a stochastic Galerkin projection can be used to transform the (stochastic) governing equations to a set of deterministic equations that can be readily discretized via standard numerical techniques. Although such a Galerkin approach is effective in many problems, cf. [10,**?**], its application to hyperbolic problems has been limited as of now. We believe that the primary reason is that the properties of the system of equations resulting from a Galerkin projection is not fully understood. (When the uncertainty does not change the direction of the characteristics, the Galerkin system can be shown to be hyperbolic and solved in a straightforward manner [3].)

We discuss in this paper the application of the gPC Galerkin method to the simulations of hyperbolic systems that contain uncertainties. In general these uncertainties may enter through initial conditions, boundary conditions or through uncertainties in the coefficients of the problem. Here we deal with the case that the coefficients are functions of random variables. In particular we use a scalar wave equation as a model and study the situation in which the inflow-outflow conditions change as a function of a random variable. The problem is whether it is possible to impose boundary conditions on the deterministic system, consistent with the boundary conditions of the original equation.

We show, in this paper, that the deterministic system is a symmetric hyperbolic system with positive as well as negative eigenvalues. A consistent and stable method of imposing the boundary conditions is outlined. The boundary conditions are not satisfied exactly at the boundaries but rather to the order of the scheme. Convergence of the scheme is established.

The paper is organized as following. In Section 12 we present the model problem of a scalar hyperbolic equation where the wave speed is a random variable. A consistent set of boundary conditions are presented for the deterministic system resulted from a gPC Galerkin procedure, and we prove convergence of the scheme. In Section 13 we

present numerical results to support the theory.

12   Model problem: Scalar Wave Equation with Uncertainty

A simple scalar equation that illustrates the difficulties in applying the (generalized) Polynomial Chaos to hyperbolic equations is:

$$\frac{\partial u(x,t,y)}{\partial t} = c(y)\frac{\partial u(x,t,y)}{\partial x}, \quad x \in (-1,1), \quad t > 0, \tag{81}$$

where $c(y)$ is a random transport velocity of a random variable $y \in \Omega$ in a properly defined complete random space with event space Ω and probability distribution function $\rho(y)$. With this the expectation of a given function is $\mathbb{E}[f(y)] = \int f(y)\rho(y)dy$. At this stage we would like to mention that we can consider (81) as a system where c is a symmetric matrix and obtain similar results. For simplicity we stay with the example above to highlight the fundamental properties. The physical domain is bounded, $(-1,1)$ upon proper scaling, so that we can study the effects of boundary conditions.

The initial condition is given by

$$u(x,0,y) = u_0(x,y). \tag{82}$$

The boundary conditions are more complicated as they depend on the sign of the random transport velocity $c(y)$. A well posed set of boundary conditions is given by:

$$u(1,t,y) = u_R(t,y), \qquad c(y) > 0,$$
$$\tag{83}$$
$$u(-1,t,y) = u_L(t,y), \qquad c(y) < 0.$$

Equations (81)–(83) complete the setup of the problem.

12.1 Polynomial Chaos Galerkin Approach

Following the standard gPC expansion, we assume that $u(x, t, y)$ is sufficiently smooth in y and has a converging expansion of the form

$$u(x, t, y) = \sum_{k=0}^{\infty} \hat{u}_k(x, t) P_k(y), \tag{84}$$

where the polynomials $P_k(y)$ correspond the distribution of the random variable y and satisfy the following orthogonality relation

$$\mathbb{E}[P_k P_l] = \int P_k(y) P_l(y) \rho(y) dy = \delta_{kl}, \quad \forall k, l, \tag{85}$$

where δ_{kl} is the Kronecker delta function. Note the polynomials are normalized. The commonly seen correspondences between the polynomials $P_k(y)$ and the distribution of the random variable y include Hermite-Gaussian (the original PC expansion), Legendre-uniform, Laguerre-Gamma, etc., cf, [32,?]. For simplicity we will discuss in this paper the case of random variable y with beta distribution in $(-1, 1)$ (upon proper scaling). In this case the expansion functions P_k are the (normalized) Jacobi polynomials. (Note this includes the special case of Legendre polynomials with uniformly distributed random variable y.) For the converged series (84), we also assume that the expansion coefficients decay fast asymptotically, i.e.,

$$\|\hat{u}_j(x, t)\|_1^2 \leq \frac{K}{j^{2m}}, \quad j \gg 1, \tag{86}$$

where $K, m > 0$ are constants and the $\| \cdot \|_1$ norm is defined as

$$\|\hat{u}_j(x, t)\|_1^2 = \int_{-1}^{1} \left[\hat{u}_j^2 + \left(\frac{\partial \hat{u}_j}{\partial x} \right)^2 \right] dx. \tag{87}$$

We also use $\| \cdot \|_2$ to denote the standard L_2 norm, i.e., $\|f(x)\|_2^2 = \int_{-1}^{1} f^2(x) dx$.

By utilizing the expansion (84) and employing a Galerkin projection, it is straightforward to verify that the coefficients $\hat{u}_j(x, t)$ satisfy the following infinite system of equations

$$\frac{\partial \hat{u}_j(x,t)}{\partial t} = \sum_{k=0}^{\infty} a_{j,k} \frac{\partial \hat{u}_k(x,t)}{\partial x} \qquad j = 0, \ldots, \infty \tag{88}$$

$$a_{j,k} = \int_{-1}^{1} c(y) P_j(y) P_k(y) \rho(y) dy. \tag{89}$$

The equations for the first $(N+1)$ coefficients can be written as

$$\frac{\partial \hat{u}_j(x,t)}{\partial t} = \sum_{k=0}^{N} a_{j,k} \frac{\partial \hat{u}_k(x,t)}{\partial x} + \sum_{k=N+1}^{\infty} a_{j,k} \frac{\partial \hat{u}_k(x,t)}{\partial x}, \quad j = 0, \ldots, N. \tag{90}$$

In the gPC Galerkin method we seek an approximation to the true solution via a finite-term gPC expansion

$$v(x,t,y) = \sum_{k=0}^{N} \hat{v}_k(x,t) P_k(y) \tag{91}$$

and project

$$\frac{\partial v(x,t,y)}{\partial t} - c(y) \frac{\partial v(x,t,y)}{\partial x} = 0$$

onto the subspace spanned by the first $(N+1)$ gPC basis polynomials and obtain the following system

$$\frac{\partial \hat{v}_j(x,t)}{\partial t} = \sum_{k=0}^{N} a_{j,k} \frac{\partial \hat{v}_k(x,t)}{\partial x}, \qquad j = 0, \ldots, N, \tag{92}$$

where $a_{j,k}$ are defined as in (89). If we denote by $\mathbf{A}$ the $(N+1) \times (N+1)$ matrix whose entries are $\{a_{j,k}\}_{0 \leq j,k \leq N}$ and $\mathbf{v} = (\hat{v}_0, \cdots, \hat{v}_N)^T$ a vector of length $(N+1)$, then system (92) can be written as

$$\frac{\partial \mathbf{v}(x,t)}{\partial t} = \mathbf{A} \frac{\partial \mathbf{v}(x,t)}{\partial x}. \tag{93}$$

Note that from the definition $a_{j,k} = a_{k,j}$, i.e., $\mathbf{A} = \mathbf{A}^T$, the system (93) is therefore *symmetric hyperbolic*, this is consistent with the fact that the original equation (81) is hyperbolic for each realization of y.

A less trivial question is the nature of the inflow-outflow boundary conditions. The boundary conditions for the original scalar equation (81) depend on the particular realization of the random variable y (see (83)). However upon the Galerkin projection in the random dimension the deterministic system (93) is independent of y. In Theorem 1 we investigate how the inflow-outflow conditions are reflected in the system (93).

Theorem 1:

Consider the deterministic system (93) where the coefficients are defined in (89). Then if $c(y) \geq 0$ (reps. $c(y) \leq 0$) for all y, then the eigenvalues of $\mathbf{A}$ are all non-negative (reps. non-positive); if $c(y)$ changes sign, i.e., $c(y) > 0$ for some y and $c(y) < 0$ for some other y, then $\mathbf{A}$ has both positive and negative eigenvalues for sufficiently large N.

Proof:

First let us consider the case of $c(y) \geq 0$.

Let $\beta(y)$ be a random variable with an expansion $\beta(y) = \sum_{k=0}^{N} b_k P_k(y)$. Let $\mathbf{b} = (b_0, \cdots, b_N)^T$ be the coefficient vector with length $(N+1)$. Note here $\mathbf{b}$ is an arbitrary vector. Then

$$\mathbf{b}^T \mathbf{A} \mathbf{b} = \sum_{j=0}^{N} \sum_{k=0}^{N} b_j a_{j,k} b_k$$

$$= \sum_{j=0}^{N} \sum_{k=0}^{N} b_j \left(\int_{-1}^{1} c(y) P_j(y) P_k(y) \rho(y) dy \right) b_k$$

$$= \int_{-1}^{1} \beta^2(y) c(y) \rho(y) dy.$$

Since $c(y)$ is non-negative

$$\mathbf{b}^T \mathbf{A} \mathbf{b} \geq 0$$

for all $\mathbf{b}$, thus all the eigenvalues of $\mathbf{A}$ are non-negative. The case of $c(y) \leq 0, \forall y$ follows similarly.

A more interesting case is when $c(y)$ changes sign. Let us devide the domain Ω where y belongs into the following non-overlapping open sets: $\Omega^+ = \Omega_1 \cup \Omega_2$ be defined as the subdomain of y where $c(y) > 0$ and Ω_3 is the subdomain of y in which $c(y) \leq 0$. Let us also define $\gamma(y)$ be a smooth function such that

$$\gamma(y) > \delta, \qquad y \in \Omega_1, \tag{94}$$
$$0 < \gamma(y) \leq \delta, \qquad y \in \Omega_2, \tag{95}$$
$$\gamma(y) = 0, \qquad y \in \Omega_3. \tag{96}$$

Let $\beta_N(y)$ be the best polynomial approximation of degree N to $\sqrt{\gamma(y)}$ such that

$$\max_y |\beta_N^2(y) - \gamma(y)| \leq \epsilon, \tag{97}$$

where N is sufficiently large such that

$$\epsilon < \delta \frac{\int_{\Omega_1} c(y)\rho(y)dy}{\int_\Omega |c(y)|\rho(y)dy}. \tag{98}$$

Then

$$\int_\Omega \beta_N^2(y)c(y)\rho(y)dy = \int_{\Omega^+} \gamma(y)c(y)\rho(y)dy + \int_{\Omega^+} (\beta_N^2(y) - \gamma(y))c(y)\rho(y)dy$$
$$+ \int_{\Omega_3} \beta_N^2(y)c(y)\rho(y)dy$$
$$\geq \int_{\Omega_1} \gamma(y)c(y)\rho(y)dy - \left|\int_{\Omega^+} (\beta_N^2(y) - \gamma(y))c(y)\rho(y)dy\right|$$
$$- \left|\int_{\Omega_3} \beta_N^2(y)c(y)\rho(y)dy\right|.$$

Now
$$\left|\int_{\Omega_3} \beta_N^2(y)c(y)\rho(y)dy\right| \leq \epsilon \int_{\Omega_3} |c(y)|\rho(y)dy$$

and
$$\left|\int_{\Omega^+} (\beta_N^2(y) - \gamma(y))c(y)\rho(y)dy\right| \leq \epsilon \int_{\Omega^+} |c(y)|\rho(y)dy$$

and therefore
$$\int_\Omega \beta_N^2(y)c(y)\rho(y)dy > 0$$

under the condition (98). Thus there exists a polynomial $\beta_N(y)$ with expansion coefficients $\mathbf{b} = (b_0, \cdots, b_N)^T$ such that $\mathbf{b}^T \mathbf{A} \mathbf{b}$ is positive. Similarly, if $c(y)$ is negative in a subinterval there exists a polynomial $\beta_N(y)$ with sufficiently large N such that $\int_{-1}^{1} \beta_N^2(y) c(y) \rho(y) dy$ is negative. Thus the matrix $\mathbf{A}$ has positive and negative eigenvalues. This concludes the proof.

12.3   Boundary Conditions and Convergence

We now turn to the issue of imposing the boundary conditions. Since $\mathbf{A}$ is symmetric there is an orthogonal matrix $\mathbf{S}^T = \mathbf{S}^{-1}$ such that

$$\mathbf{S}^T \mathbf{A} \mathbf{S} = \Lambda,$$

where Λ is a diagonal matrix whose entries on the eigenvalues of $\mathbf{A}$, i.e.,

$$\Lambda = \mathrm{diag}(\lambda_0, \ldots, \lambda_{j_+}, \ldots, \lambda_{j_-}, \ldots, \lambda_N).$$

Here the positive eigenvalues occupy indices $j = 0, \ldots, j_+$, the negatives ones $j = j_-, \ldots, N$, and the rest, if exist, are zeros. Obviously, $j_+, j_- \leq N$.

Denote by $\mathbf{q} = (q_0, \ldots, q_N)^T = \mathbf{S}^T \mathbf{v}$, i.e.,

$$q_j(x, t) = \sum_{k=0}^{N} s_{k,j} \hat{v}_k(x, t),$$

where $s_{j,k}$ are the entries for $\mathbf{S}$, then we obtain

$$\frac{\partial \mathbf{q}(x, t)}{\partial t} = \Lambda \frac{\partial \mathbf{q}(x, t)}{\partial x}. \tag{99}$$

The boundary conditions of this diagonal system are determined by the sign of the eigenvalues, i.e., we need to specify

$$q_j(1, t) = \sum_{k=0}^{N} s_{k,j} \hat{u}_k(1, t), \qquad j = 0, \ldots, j_+,$$

$$\tag{100}$$

$$q_j(-1, t) = \sum_{k=0}^{N} s_{k,j} \hat{u}_k(-1, t), \qquad j = j_-, \ldots, N.$$

Here the coefficients $\hat{u}_k$ at the boundaries are determined by the exact gPC projection of the boundary conditions of u, i.e.,

$$u_R(t, y) = \sum_{j=0}^{\infty} \hat{u}_k(1, t) P_k(y),$$

$$u_L(t, y) = \sum_{j=0}^{\infty} \hat{u}_k(-1, t) P_k(y).$$

Subsequently the boundary conditions for the gPC Galerkin system of equations (93) are specified as
$$\mathbf{v}(1, t) = \mathbf{Sq}(1, t), \quad \mathbf{v}(-1, t) = \mathbf{Sq}(-1, t). \tag{101}$$
Note the above specification of boundary conditions via (100) and (101) implicitly satisfy the following relation

$$\sum_{k=0}^{N} s_{k,j} \hat{v}_k(1, t) = \sum_{k=0}^{N} s_{k,j} \hat{u}_k(1, t), \qquad j = 0, \dots, j_+,$$

$$\sum_{k=0}^{N} s_{k,j} \hat{v}_k(-1, t) = \sum_{k=0}^{N} s_{k,j} \hat{u}_k(-1, t), \qquad j = j_-, \dots, N.$$

For vanishing eigenvalues, if they exist, no boundary conditions are required.

Theorem 2

Consider the hyperbolic equation equation (81) where y is a random variable with beta distribution in $(-1, 1)$. Let $u(x, t, y)$ be the solution of (81) whose exact gPC expansion is (84) and let $v(x, t, y)$ be the $(N + 1)$-term gPC solution (91) solved via the Galerkin system (93) with boundary conditions given in (101). Then for any finite time t
$$\mathbb{E}\left[\|u - v\|_2^2\right] = \sum_{j=0}^{N}\left(\int_{-1}^{1}(\hat{u}_j(x, t) - \hat{v}_j(x, t))^2 dx\right) \leq \frac{K}{N^{2m-1}} t. \tag{102}$$
Note the linear growth in time.

Proof

Let
$$e_j(x,t) = \hat{u}_j(x,t) - \hat{v}_j(x,t), \quad j = 0, \ldots, N.$$
¿From (90) and (92) we have

$$\frac{\partial e_j(x,t)}{\partial t} = \sum_{k=0}^{N} a_{j,k} \frac{\partial e_k(x,t)}{\partial x} + \sum_{k=N+1}^{\infty} a_{j,k} \frac{\partial \hat{u}_k(x,t)}{\partial x}, \quad j = 0, \ldots, N. \tag{103}$$

Denote by $\mathbf{e} = (e_0, \ldots, e_N)^T$ and let $\mathbf{d} = \mathbf{S}^T \mathbf{e}$, then we obtain

$$\frac{\partial \mathbf{d}}{\partial t} = \Lambda \frac{\partial \mathbf{d}}{\partial x} + \mathbf{R}, \tag{104}$$

where the residual vector $\mathbf{R} = (R_0, \cdots, R_N)^T$ is

$$R_j(x,t) = \sum_{l=0}^{N} \sum_{k=N+1}^{\infty} s_{l,j} a_{k,l} \frac{\partial \hat{u}_k}{\partial x}. \tag{105}$$

By multiplying (104) by $\mathbf{d}^T$ and integrating in x one gets

$$\frac{1}{2} \frac{d}{dt} \int_{-1}^{1} \mathbf{d}^T \mathbf{d} \, dx = \frac{1}{2} \sum_{j=0}^{N} \lambda_j \left(d_j^2(1,t) - d_j^2(-1,t) \right) + \int_{-1}^{1} \mathbf{d}^T \mathbf{R} \, dx \tag{106}$$

¿From the boundary conditions (101) it follows that if $\lambda_j > 0$ then $d_j(1,t) = 0$ and if $\lambda_j < 0$ then $d_j(-1,t) = 0$. Thus the first term in the right hand side of the above equation is negative. This leads to

$$\frac{1}{2} \frac{d}{dt} \int_{-1}^{1} \mathbf{d}^T \mathbf{d} \, dx \equiv \frac{1}{2} \frac{d}{dt} \|\mathbf{d}\|^2 \leq \|\mathbf{d}\| \cdot \|\mathbf{R}\|,$$

where

$$\|\mathbf{R}\|^2 = \sum_{j=0}^{N} \int_{-1}^{1} R_j^2(x,t) dx$$

and $\|\mathbf{d}\|$ is defined similarly.

Thus

$$\frac{d}{dt} \|\mathbf{d}\| \leq \|\mathbf{R}\|$$

and
$$\|\mathbf{d}(x,t)\| \leq \max_{t \geq 0} \|\mathbf{R}\| \cdot t$$

Since the matrix $\mathbf{S}$ is unitary and the elements of the matrix $\mathbf{A}$ are bounded then

$$\|\mathbf{R}\|^2 \leq \sum_{j=N+1}^{\infty} \|\hat{u}_j\|_1^2 \tag{107}$$

and the proof is established under assumption (86).

13 Numerical Results

In this section we present a few numerical examples to support the theoretical results derived above. In all of the following computations, we have used sufficiently fine resolutions in physical space and time domain, such that the spatial and temporal errors are negligible. In all computations, y is a random variable uniformly distributed in $(-1, 1)$ and thus $P_k(y)$ are (normalized) Legendre polynomials.

13.1 Periodic Problem

We first consider problem (81) with a periodic boundary condition in physical space. Subsequently the gPC Galerkin system (93) requires periodic boundary conditions that can be trivially implemented. Therefore no errors will be induced by specifying boundary conditions via (101). Let us consider

$$\begin{aligned} u_t(x,t,y) &= yu_x(x,t,y),\ 0 < x < 2\pi, t \geq 0, \\ u(x,0,y) &= \cos(x), \qquad 0 < x < 2\pi, \end{aligned} \tag{108}$$

The exact solution is $u_{\text{ex}} = \cos(x - yt)$. In Figure 25 we plot the evolution of the mean square solution $\mathbb{E}[\|u\|_2^2] = \int \int_{-1}^1 u^2(x,t,y)\rho(y)dydx$ and its numerical solution via gPC Galerkin method. We observe that there is a finite time where the numerical solutions lose accuracy, i.e., errors become $O(1)$. The size of the time domain in which the errors remain small grows almost linearly as the orders of gPC expansion are increased. This observation can be cross-examined by comparing the mean-square errors at different time level, as shown in Figure 26. We observe that with sufficiently high

orders of gPC expansions, exponential error convergence can be achieved. However, as time increases, the critical orders of expansions, beyond which errors start to decay exponentially fast, increase linearly. All of these results support the convergence analysis (102) where a linear error growth in time exists.
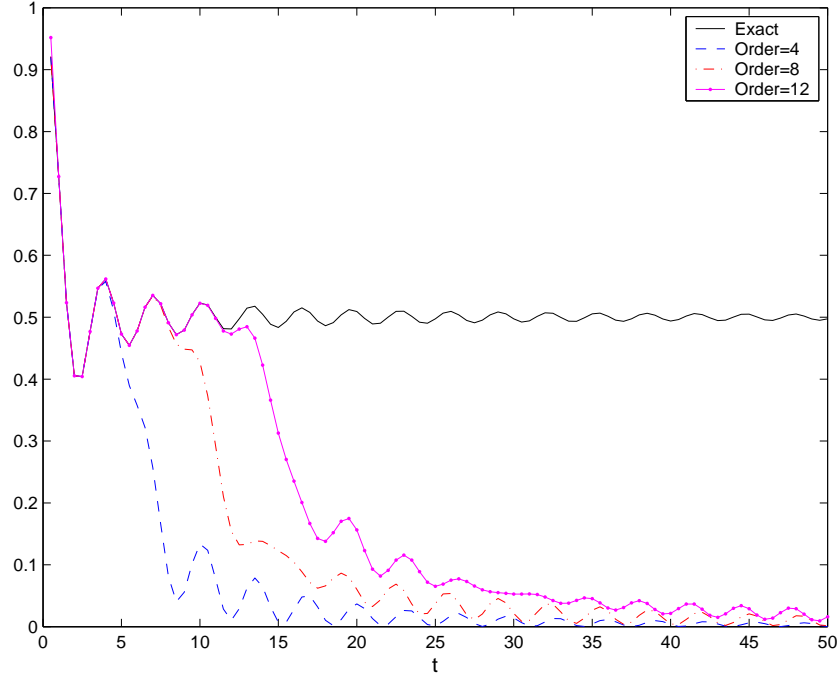

Fig. 25. Evolution of errors in mean-square norm over time.

13.2 Boundary Conditions and Discontinuity in Random Space

We now study a wave equation with a random wave speed that changes signs and also contains a discontinuity in the random space

$$
\begin{aligned}
u_t &= c(y)u_x, & -1 \le x \le 1,\ t > 0, \\
u(x,0,y) &= \sin(\kappa x), & -1 \le x \le 1,\ y > 0, \\
u(x,0,y) &= \sin(2\kappa x), & -1 \le x \le 1,\ y < 0.
\end{aligned}
\tag{109}
$$

72
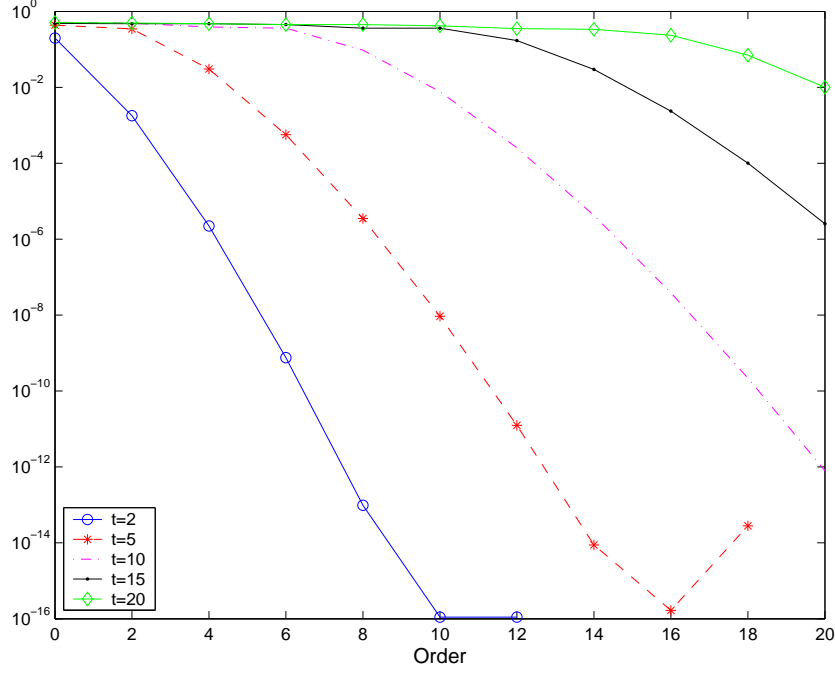
Fig. 26. Convergence of mean-square errors with increasing orders.

Here $c(y) = \sigma y$ with $0 < \sigma < 1$ controlling the variability of the random input and $\kappa > 0$ is a real constant. We prescribe boundary conditions as

$$
\begin{aligned}
u(1, t, y) &= \sin[\kappa(1 + c(y)t)], & y &> 0, \\
u(-1, t, y) &= \sin[2\kappa(-1 + c(y)t)], & y &< 0.
\end{aligned}
\tag{110}
$$

The exact solution of (109)–(110) is $u_e(x, t, y) = \sin[\kappa(x + c(y)t)]$ for $y > 0$ and $u_e(x, t, y) = \sin[2\kappa(x + c(y)t)]$ for $y < 0$. Note the solution is discontinuous in term of y, although each realization of y is a smooth function in x.

The numerical solutions are solved with $\sigma = 0.5$ and $\kappa = 1$. The numerical boundary conditions are implemented via the eigenvalue analysis (101). For numerical solutions of gPC order N, we examine three error measures: error in mean $e_{\mathrm{mean}}(N, t) = \max_x |\mathbb{E}(v) - \mathbb{E}(u_e)|$, error in standard deviation (STD) $e_{\mathrm{std}}(N, t) = \max_x |\sigma_v - \sigma_{u_e}|$, and the mean-square error $e_2(N, t) = \max_x (\mathbb{E}[(v - u_e)^2])^{1/2}$. Numerical simulations are conducted up to $t = 1$, and we define convergence rate as $r(N) = [\ln(e(N)) - \ln(e(M))] / [\ln(N) - \ln(M)]$ for expansion orders $N > M \geq 1$, where e is one of the three error measures.

Figure 27 shows the convergence of the three errors with increasing order of Legendre expansions. In this case, we observe different convergence properties between even and

73

odd orders of expansions, although they appear to have similar asymptotic convergence rate. Note that such different error behaviors between even and odd expansions can be seen in classical spectral methods, cf. [14]. The errors, along with their convergence rates, are tabulated in Table XI and Table XII, for odd and even orders of expansions, respectively. No exponential convergence is achieved, as opposed to that in the earlier examples. Also, the weak error measures (error in mean and error in STD) converge more rapidly than the strong error measure in term of mean-square.
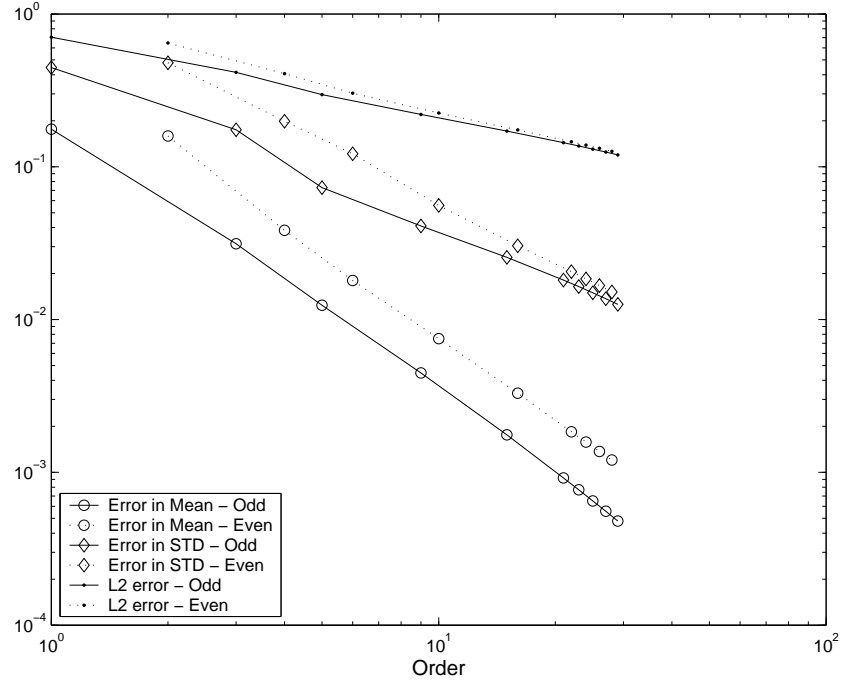

Fig. 27. Errors for odd and even orders of Legendre-chaos expansions.

The slower convergence is due to the discontinuity in random space, and is manifested in Fig. 28, where the numerical solution $v(x, t, y)$ is shown at location $x = 0.454$ with $N = 21$ order of expansion. Fig. 28(a) shows the approximation at $t = 0$, i.e., the initial condition, and Fig. 28(b) shows the numerical solution at $t = 1$. The Gibbs' oscillations around the discontinuity at $y = 0$ are clearly visible.

14 Summary

The properties of (generalized) Polynomial Chaos method for uncertainty analysis of hyperbolic equations are studied. We show, via a simple model problem of a scalar

Table XI

Errors for odd-order Legendre-chaos expansions and their convergence rate.

N	e_{mean}	r_{mean}	e_{std}	r_{std}	e_2	r_2
1	0.1761	–	0.4460	–	0.7044	–
3	3.137(-2)	1.57	0.1747	0.85	0.4147	0.48
5	1.241(-2)	1.82	7.300(-2)	1.71	0.2965	0.66
9	4.470(-3)	1.74	4.095(-2)	0.98	0.2202	0.51
15	1.758(-3)	1.83	2.553(-2)	0.92	0.1713	0.49
21	9.188(-4)	1.93	1.815(-2)	1.01	0.1438	0.52
23	7.680(-4)	1.97	1.644(-2)	1.08	0.1368	0.55
25	6.503(-4)	2.00	1.498(-2)	1.12	0.1305	0.56
27	5.564(-4)	2.03	1.370(-2)	1.16	0.1248	0.58
29	4.803(-4)	2.06	1.257(-2)	1.20	0.1195	0.60

Table XII

Errors for even-order Legendre-chaos expansions and their convergence rate.

N	e_{mean}	r_{mean}	e_{std}	r_{std}	e_2	r_2
2	0.1589	–	0.4791	–	0.6457	–
4	3.841(-2)	2.05	0.1985	1.27	0.4065	0.67
6	1.803(-2)	1.87	0.1215	1.21	0.3030	0.72
10	7.503(-3)	1.72	5.588(-2)	1.52	0.2249	0.58
16	3.295(-3)	1.75	3.042(-2)	1.29	0.1741	0.54
22	1.843(-3)	1.82	2.058(-2)	1.23	0.1457	0.56
24	1.577(-3)	1.79	1.846(-2)	1.25	0.1386	0.58
26	1.370(-3)	1.76	1.668(-2)	1.27	0.1321	0.59
28	1.204(-3)	1.74	1.516(-2)	1.29	0.1263	0.61

wave equation with random wave speed, some prominent features of the resulting deterministic system of equations obtained by a Galerkin projection in random space. We proved the existence of both positive and negative eigenvalues when the wave speed changes sign in random space and presented a consistent and stable method for imposing boundary conditions for the deterministic equations. The gPC Galerkin method, with the proper boundary treatment, is shown to be convergent. Furthermore, the error contains a linear growth in time which is independent of the boundary conditions. We remark that although the linear wave equation considered here
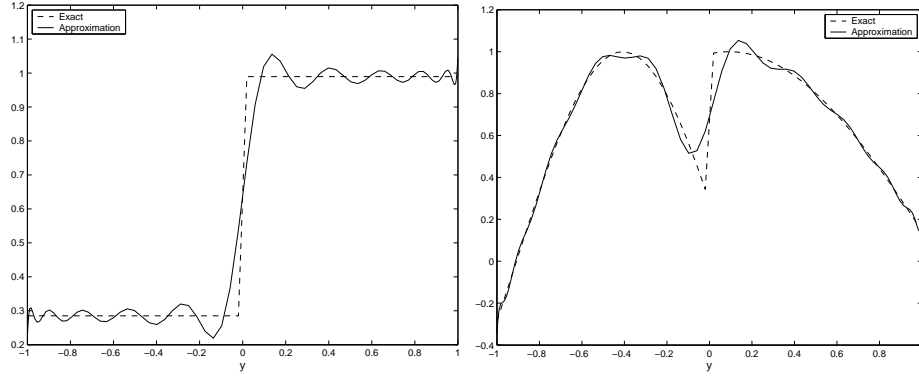
Fig. 28. Numerical approximations of $u_N(x, t, y)$ at $x = 0.454$ with $N = 21$. (a) $t = 0$; (b) $t = 1$.

is rather simple, it possesses one of the key issues in applying gPC Galerkin method to hyperbolic problems – the proper way to enforce boundary conditions when the characteristic wave changes directions in random space. This issue is addressed here and it opens up the possibility of applying gPC Galerkin method to other hyperbolic problems with uncertainty, e.g., nonlinear wave equations, Maxwell equations, etc.

Acknowledgment/Disclaimer

References

1. D. Gottlieb and S. A. Orszag, *Numerical Analysis of Spectral Methods: Theory and Applications*, CBMS conference Series in Applied Mathematics 26, SIAM, (1977)

2. G. S. Jiang and C-W Shu, Efficient Implementation of Weighted ENO Schemes, Journal of Computational Physics 126 (1996)

3. A. Harten, High Resolution Schemes for Hyperbolic Conservation Laws, Journal of Computational Physics 49 (1983)

4. K. R. Meadows, A. Kumar and M. Y. Hussaini, A Computational Study on the Interaction Between a Vortex and a Shock Wave, AIAA Paper 89-104 (1989)

5. R. D. Richtmyer, Taylor Instability in Shock Acceleration of Compressible Fluids, Comm. Pure Appl. Math, 13, pp. 297-319 (1960)

6. E. E. Meshkov Instability of a Shock Wave Accelerated Interface between Two Gases, NASA, F-13:074 (1970)

Personnel Supported During Duration of Grant

David Gottlieb -Ford Foundation Professor, Brown University.

Wai Sun Don - Research Full Professor, Brown University.

Jessica Libertiny - PhD 2008.

Publications

B. Costa & W. S. Don, *Hybrid Central-WENO Finite Difference Methods for Conservation Laws*, Journal of Computational and Applied Mathematics, accepted, 2006.

B. Costa & W. S. Don, *Multi-Domain Hybrid Spectral-WENO Methods for Hyperbolic Conservation Laws*, Journal of Computational Physics, under revision, 2006.

B. Costa, W. S. Don, D. Gottlieb & R. Sendersky, *Two-Dimensional Multi-Domain Hybrid Spectral-WENO Methods for Conservation Laws*, Communication in Computational Physics, 1 (2006), pp. 548-574

R. Borges, B. Costa & W. S. Don, *An Improved Weighted Essentially Non-Oscillatory Scheme for Hyperbolic Conservation Laws*, Journal of Computational Physics, submitted, 2006.

M. Latini, O. Schilling & W. S. Don, *Effects of WENO flux reconstruction order and spatial resolution on reshocked two-dimensional Richtmyer-Meshkov instability*, Journal of Computational Physics, 2007.

M. Latini, O. Schilling & W. S. Don, *High-resolution simulations and modeling of reshocked single-mode Richtmyer-Meshkov instability : Comparison to experimental data and to amplitude growth model predictions*, Physics of Fluids, 19, 2, 2007.

M. Latini, O. Schilling & W. S. Don, *Physics of reshock and mixing in single-mode Richtmyer-Meshkov instability*, Physics Reviews E, 76, 2007.

A. Kanevsky, M. H. Carpenter, D. Gottlieb & J. S. Hesthaven, *Implicit-Explicit Runge-Kutta Discontinuous Galerkin Methods and Applications*, Journal of Computational Physics, 225, 2, 2007.

W. S. Don, D. Gottlieb & J. H. Jung, *A weighted multi-domain spectral penalty method with inhomogeneous grid for supersonic injective cavity flows*, Communication in Computational Physics, under revision.

Honors & Awards Received

David Gottlieb received the NASA group achievement award in 1992. He was given the Ford Foundation chair at Brown University in 1993. He received an honorary doctorate from the university of Paris 1994 and from the university of Uppsala, Sweden in 1996. He is a member of National Academy of Science and Honary President of ICOSAHOM.

AFRL Point of Contact

Dr. Datta V. Gaitonde, AFRL/VAAC, 2210 Eighth Street, WPAFB, OH 45433